

Connectomic analysis reveals an interneuron with an integral role in the retinal circuit for night vision

Silvia JH Park^{1†}, Evan E Lieberman^{2†}, Jiang-Bin Ke², Nao Rho², Padideh Ghorbani², Pouyan Rahmani¹, Na Young Jun¹, Hae-Lim Lee³, In-Jung Kim¹, Kevin L Briggman⁴, Jonathan B Demb^{1,3,5*}, Joshua H Singer^{2*}

¹Department of Ophthalmology & Visual Science, Yale University, New Haven, United States; ²Department of Biology, University of Maryland, College Park, United States; ³Department of Cellular & Molecular Physiology, Yale University, New Haven, United States; ⁴Circuit Dynamics and Connectivity Unit, National Institute of Neurological Disorders and Stroke, National Institutes of Health, Bethesda, United States; ⁵Department of Neuroscience, Yale University, New Haven, United States

Abstract Night vision in mammals depends fundamentally on rod photoreceptors and the well-studied rod bipolar (RB) cell pathway. The central neuron in this pathway, the All amacrine cell (AC), exhibits a spatially tuned receptive field, composed of an excitatory center and an inhibitory surround, that propagates to ganglion cells, the retina's projection neurons. The circuitry underlying the surround of the All, however, remains unresolved. Here, we combined structural, functional and optogenetic analyses of the mouse retina to discover that surround inhibition of the All depends primarily on a single interneuron type, the NOS-1 AC: a multistratified, axon-bearing GABAergic cell, with dendrites in both ON and OFF synaptic layers, but with a pure ON (depolarizing) response to light. Our study demonstrates generally that novel neural circuits can be identified from targeted connectomic analyses and specifically that the NOS-1 AC mediates long-range inhibition during night vision and is a major element of the RB pathway.

***For correspondence:**

jonathan.demb@yale.edu (JBD);
jhsinger@umd.edu (JHS)

[†]These authors contributed equally to this work

Competing interests: The authors declare that no competing interests exist.

Funding: See page 23

Received: 16 February 2020

Accepted: 27 April 2020

Published: 15 May 2020

Reviewing editor: Fred Rieke, University of Washington, United States

© Copyright Park et al. This article is distributed under the terms of the [Creative Commons Attribution License](https://creativecommons.org/licenses/by/4.0/), which permits unrestricted use and redistribution provided that the original author and source are credited.

Introduction

In dim light, vision originates with rod photoreceptors, which are sensitive enough to respond to single photons (Ingram et al., 2016; Pugh, 2018). In mammals, rod output is conveyed to ganglion cells (GCs), the retinal projection neurons, via a specialized circuit: the rod bipolar (RB) cell pathway (Demb and Singer, 2015; Famiglietti and Kolb, 1975; Field et al., 2005; Figure 1). The central neuron in the RB pathway is the All amacrine cell (AC), which receives excitatory, depolarizing input from the RBs at light stimulus onset, and is therefore an ON cell. The All provides feedforward signals that simultaneously drive depolarizing and hyperpolarizing responses in ON and OFF GC types, respectively (Figure 1; Murphy and Rieke, 2006; Strettoi et al., 1994; Strettoi et al., 1992). The circuitry of the RB pathway efficiently transforms weak sensory inputs into neural responses with high signal-to-noise ratio (Field et al., 2005) capable of guiding behavior at visual threshold (Smeds et al., 2019).

Although well-studied, several uncertainties about RB pathway function remain (Demb and Singer, 2012). Most significantly, we do not understand the cellular basis for the spatial receptive field of the All, which is composed of an excitatory center, driven by RB input, and an antagonistic, inhibitory surround. The surround is apparently generated by the activity of a spiking, GABAergic AC that makes direct inhibitory synapses with the All, but the identity of this critical interneuron and

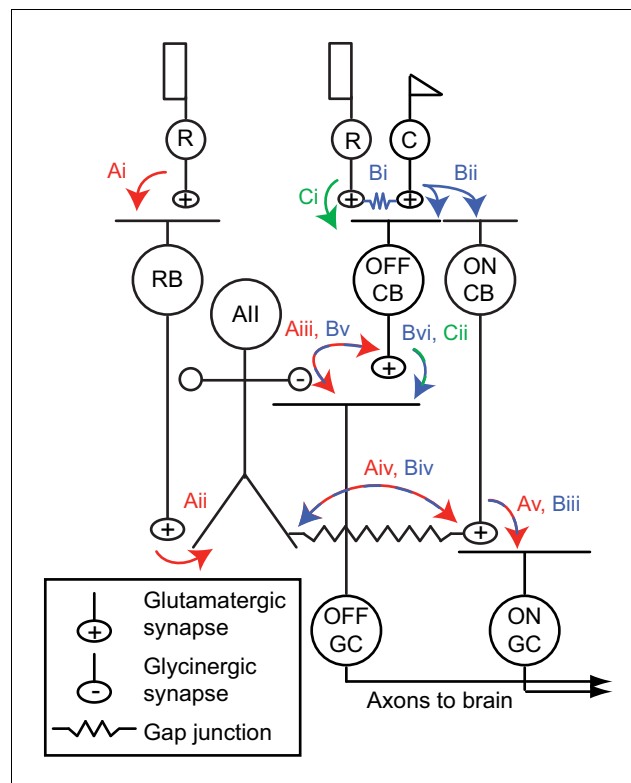


Figure 1. The mammalian retinal pathway for night vision. (Ai-Av) In red: the rod bipolar (RB) pathway of mammalian retina. Rods make synapses onto RBs (Ai), which make synapses onto the AII. Signaling from AII to ON and OFF pathways is compartmentalized by the morphology of the AII, a bistratified cell with distinct neurites in the ON and OFF sublaminae of the inner plexiform layer (IPL). (Aii). Proximal (OFF-layer) dendrites provide glycinergic synapses (Aiii) onto the terminals of some OFF cone bipolar (CB) cells [primarily type 2 CBs; (Graydon et al., 2018)] and onto the dendrites of some OFF ganglion cells (GCs), including OFF α and δ GCs as well as suppressed-by-contrast GCs (Beaudoin et al., 2019; Demb and Singer, 2012; Jacoby et al., 2015). At their distal (ON-layer) dendrites, AII are coupled by electrical synapses to the terminals of ON CBs (Aiv) (particularly type 6 CBs presynaptic to ON α GCs); depolarization of AII drives excitatory transmission to GCs, including ON α GCs (Schwartz et al., 2012) (Av). Thus, the AII mediates so-called ‘cross-over’ inhibition, whereby one pathway (ON, in this case) suppresses the other (OFF) and thereby decorrelates their outputs (Demb and Singer, 2015). (Bi-Bvi) In blue: rods are coupled electrically to cones by gap junctions (Bi), and cones make synapses onto ON and OFF CBs (Bii). Depolarization of the ON CB by the cone not only drives glutamatergic transmission to ON GCs (Biii), it also depolarizes AII via the electrical synapses (Biv) and thereby elicits glycinergic transmission to OFF GCs and perhaps OFF CBs (Bv). (Ci-Cii) In green: rods make direct chemical synapses onto some types of OFF CB (Ci), which in turn contact OFF GCs (Cii).

the retinal circuitry in which it participates remain unresolved (Bloomfield and Xin, 2000). Understanding mechanisms contributing to surround inhibition of the AII would explain how the retina encodes spatial information in dim light.

Here, we identified the major inhibitory input to the AII by combining anatomical, genetic, and electrophysiological analyses in a three-step process. One, we reconstructed ACs that provided synaptic input to AII in a volume of mouse retina imaged by scanning block-face electron microscopy [SBEM; (Denk and Horstmann, 2004)]. Two, we evaluated published descriptions of reporter mouse lines to identify genetically-accessible ACs that had the anatomical characteristics of the cells reconstructed from SBEM images. And three, we used electrophysiological recordings and genetics-based circuit analysis to demonstrate that a candidate AC, which provided the great majority of the inhibitory synaptic input to AII, exhibited a light response predicted by its anatomy and made GABAergic synapses onto AII. This spiking, GABAergic AC is a multistratified, ON AC denoted NOS-1 AC and identified in the nNOS-CreER mouse line (Zhu et al., 2014). We conclude that the NOS-1 AC is an integral component of the RB pathway and a significant source of long-range inhibition during night

vision. More generally, our study demonstrates the utility of targeted, small-scale 'connectomic' analysis for identification of novel neural circuits.

Results

Alls in the mouse retina exhibit a TTX-sensitive, GABAergic receptive field surround

The inhibitory receptive field surround of Alls has been studied extensively in the rabbit retina, where it is GABAergic and appears to be generated by spiking ACs because it is suppressed by the voltage-gated sodium channel blocker tetrodotoxin (TTX) (*Bloomfield and Xin, 2000; Xin and Bloomfield, 1999*). Here, we began by probing for the existence of a similar TTX-sensitive surround mechanism in Alls of the mouse retina (*Figure 2A*).

Alls were targeted for recording in the whole-mount retina (see Materials and methods; *Mortensen et al., 2016*), and rods were stimulated with light spots of varying diameter eliciting 10 photoisomerizations (R^*)/rod/s, an intensity that reliably activates the RB pathway (see Materials and methods). Evoked excitatory currents (voltage-clamp; $V_{\text{hold}} = E_{\text{Cl}} = -70$ mV) increased with spot diameter well beyond the physical ~ 30 μm width of the All dendritic field (*Figure 2B*). This wide receptive field of excitation is explained by electrical coupling within the All network (*Hartveit and Veruki, 2012; Xin and Bloomfield, 1999*): an excitatory current originating in surrounding Alls spreads laterally as a coupling current. Recording at $V_{\text{hold}} = E_{\text{cation}} = +5$ mV during spot presentation in control (Ames') medium yielded an evoked current comprising a mixture of genuine inhibitory current and unclamped coupling current. In the presence of TTX, the inhibitory input was suppressed, leaving the coupling current (*Figure 2A*). The difference current (Ames' – TTX; *Figure 2A*) is the isolated, TTX-sensitive, rod-driven inhibitory input, which increased as a function of spot diameter (*Figure 2C*). We observed as well that TTX exerted a mild suppressive effect on the excitatory light-evoked current, suggesting that spiking interneurons influence synaptic transmission from the presynaptic bipolar cells (*Figure 2B*).

Propagation of the All surround to downstream GCs

The surround suppression of Alls is expected to propagate to the GCs that receive input from the RB-All network. This includes three GC types that receive input from the RB pathway at or near visual threshold: the ON α GC and the OFF α and δ GCs, which exhibit high sensitivity to spatial contrast in the visual scene—similar to primate parasol cells—and project to the geniculo-cortical pathway (*Ala-Laurila et al., 2011; Ala-Laurila and Rieke, 2014; Dunn et al., 2006; Grimes et al., 2018a; Grimes et al., 2015; Grimes et al., 2014b; Grimes et al., 2018b; Ke et al., 2014; Kuo et al., 2016; Murphy and Rieke, 2006; Murphy and Rieke, 2008*). We recorded from these GC types while rods were stimulated with dim (evoking either 4 or 40 R^* /rod/s) spots of varying size; this stimulus will evoke excitatory postsynaptic currents (EPSCs) in ON α GCs and inhibitory postsynaptic currents (IPSCs) in OFF α and δ GCs that reflect the output of the RB-All network (*Murphy and Rieke, 2006; Murphy and Rieke, 2008*).

As spot diameter increased up to 2000 μm , EPSCs in ON α GCs and IPSCs in OFF α and δ GCs first increased and then decreased in amplitude, reflecting an initial increase in the receptive field center response and then subsequent surround suppression of the center response (*Figure 2D–F*). The IPSCs recorded in OFF α and δ GCs were similar, although not identical, likely reflecting shared inputs from the All combined with cell type-specific inhibitory inputs from unique AC types. Nevertheless, in all three GC types, surround suppression was blocked similarly by TTX, suggesting that it was mediated by a common presynaptic mechanism: inhibition of the All. Thus, the mouse All exhibits a TTX-sensitive receptive field surround mediated by direct inhibitory synapses and this surround is propagated to GCs. To understand the mechanism for surround inhibition, we searched for the inhibitory ACs presynaptic to the mouse All.

Anatomical identification of inhibitory synaptic inputs to Alls

We began by skeletonizing three All ACs distributed across serial block face electron microscopy (SBEM) volume k0725 [mouse retina; $50 \times 210 \times 260$ μm ; (*Ding et al., 2016*); available at https://webknossos.org/datasets/Demo_Organization/110629_k0725/view]. Alls were traced from their

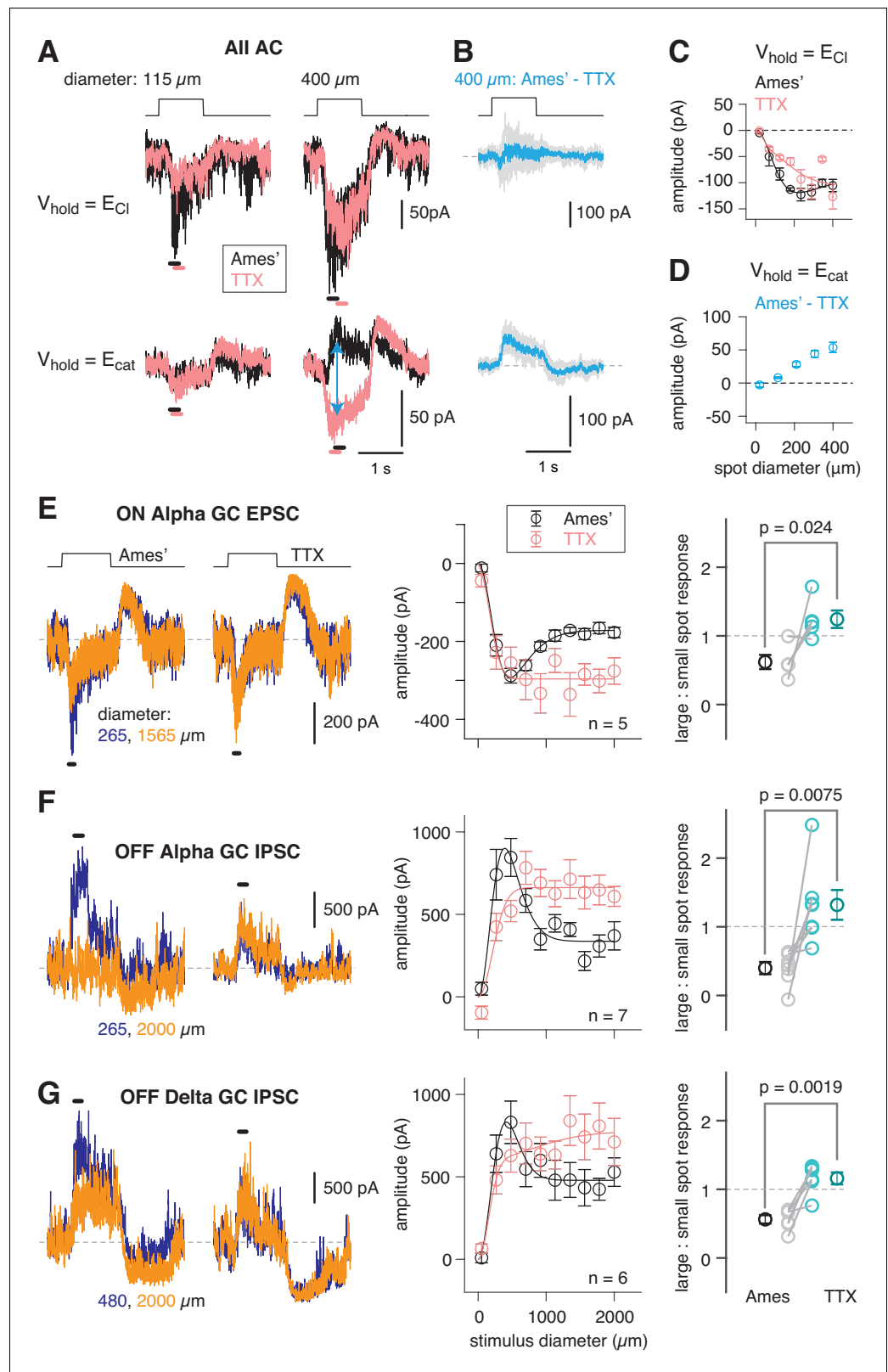


Figure 2. An inhibitory surround recorded in mouse All ACs. (A) All responses to spots of light (10 R*/rod/s, 1 s duration) with the indicated diameter in control condition (Ames' medium) and after applying TTX (1 μM). Responses were recorded at holding potentials (V_{hold}) near E_{Cl} (-70 mV; top row) and near E_{cat} ($+5$ mV; bottom row). (B) Difference current at each V_{hold} for the 400 μm spot (average of $n = 5$ cells; shaded areas). Figure 2 continued on next page

Figure 2 continued

are \pm SEM across cells as a function of time. (C) Response amplitude (measured over a 200 ms window: horizontal bars in A) to spot of variable diameter at $V_{\text{hold}} = E_{\text{Cl}}$ ($n = 5$ cells). Error bars are \pm SEM across cells. (D) Amplitude of difference current at $V_{\text{hold}} = E_{\text{cat}}$ averaged across cells. Conventions as in (C). (E) Left, light flash (dark background, two spot sizes, 4 or 40 $R^*/\text{rod}/s$ across cells)-evoked EPSCs in an ON α RGC. Under control conditions, the response is smaller for the larger diameter, illustrating the surround effect, which is blocked by TTX (1 μM). Middle, Spot stimuli of varying diameter (Ames' and TTX) elicit EPSCs; peak response amplitude measured in a time window (100–200 ms; horizontal line at left). Right, ratio of response to large (averaged over the three largest diameters) and small (chosen as the optimal spot size for each cell in the control condition) spots. A ratio <1 indicates a surround effect. The ratio increased significantly in TTX. (F) Same as (E) for IPSCs in OFF α RGCs (spot intensity, 4 $R^*/\text{rod}/s$). (G) Same as (F) for OFF δ RGCs.

locations presynaptic to dyad ribbon synapses at RB terminals that were themselves identified by morphology and position within the inner plexiform layer (IPL) (Graydon et al., 2018; Mehta et al., 2014; Pallotto et al., 2015). For each of these three Alls, we annotated all the inputs from ribbon synapses, arising from RBs, as well as all the conventional synaptic inputs, presumed to arise from inhibitory ACs (Figure 3A). Alls received substantial input to their distal (ON layer) dendrites from RBs (Table 1; Figure 3B), consistent with published descriptions (Strettoi et al., 1992; Tsukamoto and Omi, 2013). With regard to inhibitory input, it is notable that virtually all AC inputs to the All were in the inner IPL (ON layer), on the distal dendrites; the remainder of the AC inputs were on the somas and most proximal portions of the All dendrites (Table 1; Figure 3B).

For each All, we skeletonized 21 of the AC inputs to the distal dendrites to assess the morphology of the presynaptic neurons (Figure 3C1, left, and 3C2). Of the 63 AC skeletons created, 61 were of neurites, generally unbranched, that extended through the volume and appeared to be axons: each of these originated from an AC not contained in the SBEM volume (Figure 3C2). After annotating their output synapses, we determined that these axons made synapses with Alls almost exclusively; the remainder of the output was to RBs with very few synapses to ON CBs and unidentified cells (Table 2; Figure 3C1, left, and 3C2). This determination was made by tracing the postsynaptic neurites sufficiently to identify RBs from their characteristic axon terminals, which are large and make dyad synapses with presumed Alls and A17 ACs, and to identify Alls based on several characteristic features: a soma position at the border of the INL and IPL; very thick proximal dendrites; and a postsynaptic position at RB dyad synapses (see Graydon et al., 2018; Mehta et al., 2014; Strettoi et al., 1990; Strettoi et al., 1992).

These 61 axons made 130 synapses onto the three reconstructed Alls, giving rise to $\sim 25\%$ of the total inhibitory input to each All. Therefore, assuming that each axon arises from a distinct cell, most Alls receive ~ 2 inputs (i.e. ~ 130 synapses/61 axons) from each presynaptic AC; these inputs occur mostly ($\sim 80\%$) within 4 μm of RB \rightarrow All synapses (Figure 3B and C), with a median distance of 2.3 μm (Figure 3C4). Thus, the inhibitory AC inputs to the All are well positioned for shunting local excitatory RB input.

The inputs to the All somas and proximal (OFF layer) dendrites (Figure 3B and C1, right) were not considered in as much detail because these were few in number and presumed to arise from dopaminergic ACs (DACs) (Contini and Raviola, 2003; Gustincich et al., 1997; Voigt and Wässle, 1987). Indeed, when we traced 8 neurites presynaptic to the soma and proximal dendrites of a single All, we identified 113 output synapses in total, 90 (80%) of which were to neighbor Alls and 23 to other cells (Figure 3C5). The All soma appeared to be enveloped in a 'basket' of such neurites (Figure 3C6), as noted previously for DAC \rightarrow All synapses (Gustincich et al., 1997; Voigt and Wässle, 1987).

Two of the 63 AC skeletons that made inputs to the All distal dendrites could be traced to a relatively complete neuron contained within the SBEM volume (Figure 4A,B). These two ACs appeared to be of the same type and were characterized as displaced (with somas in the GC layer), multi-stratified cells, with processes in both the ON and OFF strata of the IPL.

Anatomical assessment of an AC circuit presynaptic to the All

We annotated all of the synaptic connections—inputs and outputs—made by the two ACs contained within the volume and then identified each pre- or postsynaptic partner (Figure 4A,B). Both ACs

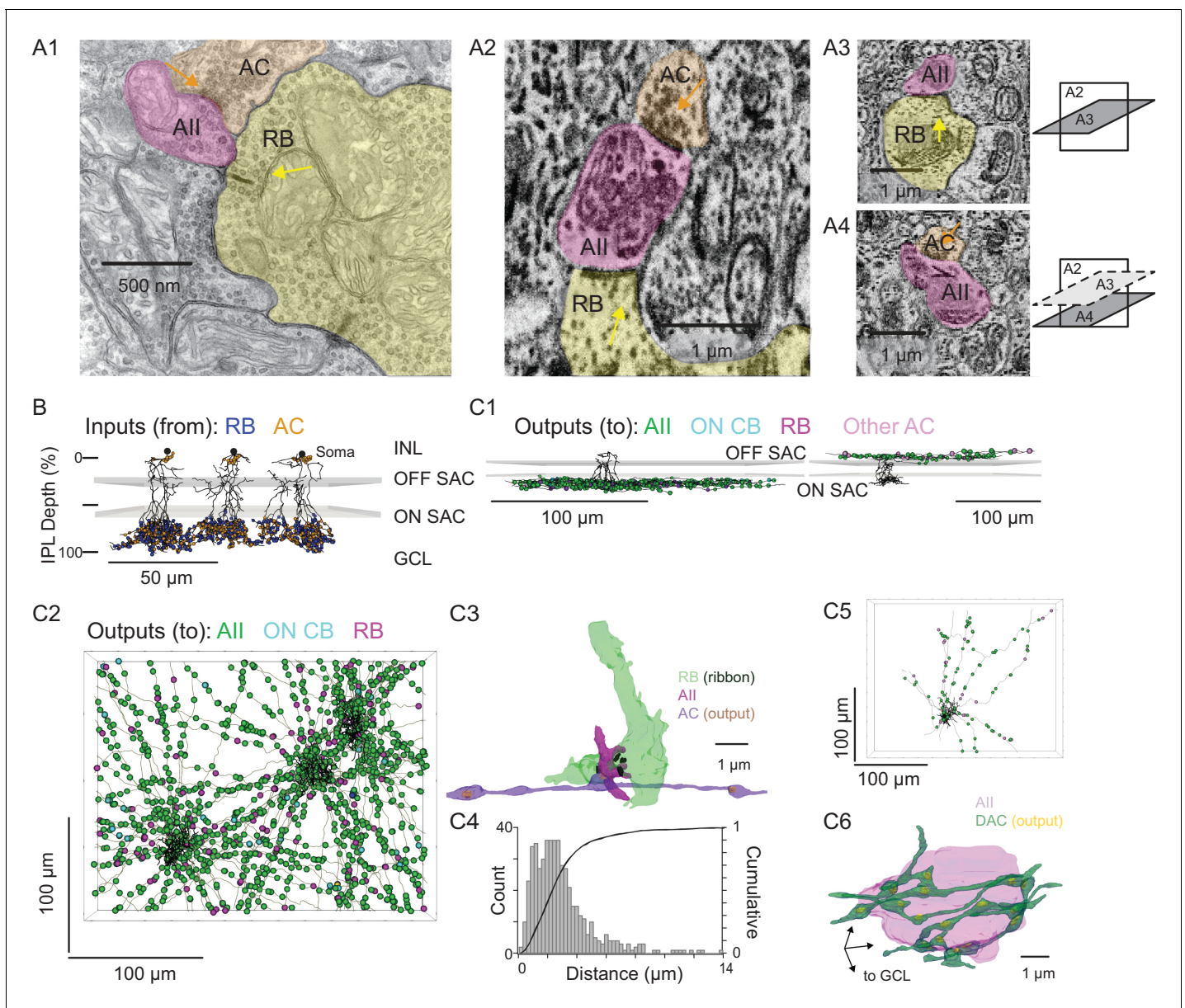


Figure 3. Anatomical characterization of AC axons presynaptic to the AII. **(A1)** A RB dyad synapse, visualized by TEM. Note the synaptic ribbon (yellow arrow) and the nearby AC input to the postsynaptic AII (orange arrow). **(A2)** A similar dyad synapse observed by SBEM. Again, the RB ribbon and AC input to the postsynaptic AII are marked with yellow and orange arrows, respectively. **(A3, A4)** Orthogonal views of the synapse illustrated in A2 showing the RB dyad (top) and the AC input to the postsynaptic AII (bottom). A3 and A4 are from different sections to illustrate the appearance of both ribbon and AC inputs in the section orthogonal to A2. This is illustrated schematically by the squares at right. **(B)** Three AII, skeletonized and annotated with either RB ribbon synapse locations or AC synapse locations. The view is from the side of the volume, representing a transverse section through the retina. The planes containing ON and OFF SAC dendrites are represented by gray rectangles. Note that the majority of AC inputs to the AII are found in the same IPL sublaminae as the RB inputs, the vitreal side of the ON SAC dendrites (from [Ding et al., 2016](#)). As well, AII receive no synaptic input from ACs in the IPL sublaminae between the ON and OFF SAC dendrites. All skeletons and annotations are contained within [Source data 1](#) and downloadable in Knossos XML format. SAC skeletons are downloadable as [Source data 3](#). **(C1)** Side view of a single AII and presynaptic neurites with output synapses annotated (right: presynaptic to distal dendrites; left: presynaptic to soma and proximal dendrites; different AII are shown in the two panels). **(C2)** An en face view, visualized from the GCL, of 3 AII (black) and 61 presynaptic axons. Note the preponderance of green circles, indicating synapses to the three reconstructed AII and other AII within the volume. Virtually every synapse that was not made with an AII was onto a RB. We observed two synapses onto these axons. Neurite annotations are contained within [Source data 1](#) and downloadable in Knossos XML format. **(C3)** Segmentation of the RB-AII-AC complex. The AC axon is thin, with occasional large varicosities containing clusters of vesicles. It makes synapses with AII, usually quite close to RB→AII ribbon synapses. In this example, the AII dendritic segment receives four ribbon inputs from the axon terminal varicosity of a RB and one conventional synaptic input from an AC. The other synapses made by this AC axon segment also are with

Figure 3 continued on next page

Figure 3 continued

Alls. (C4) Conventional and normalized cumulative histograms of distribution of nearest-neighbor distances between AC→All and RB→All synapses. (C5) An *en face* (from GCL) view of a single All and neurites presynaptic to its soma and proximal dendrites. (C6) Segmentation of an All soma and presynaptic neurites, with presynaptic active zones annotated. The image is a tilted side view; the orientation axis (lower left) indicates the relative position of the GCL.

exhibited very similar patterns of connectivity, as quantified in **Table 2**. Interestingly, the vast majority of synaptic output was to Alls (All identity confirmed as described above); a smaller but significant portion was to RBs (again, confirmed as above), with the remainder to ON CBs (which were skeletonized completely; below). We did not observe any synapses onto other ACs or onto GCs. Thus, these two ACs appear to be representatives of a singlecell type that contacts preferentially neurons in the RB pathway, specifically Alls. Given the similarity of the postsynaptic target neuron populations of these ACs and the axons reconstructed partially and described above (**Figure 3B**, left, and 3C2, 3), we believe all to be representative of the same AC type, a cell that contacts Alls preferentially and provides the vast majority of inhibitory synapses to the All.

Both ACs received very similar numbers of inputs from conventional and ribbon synapses (**Table 2**). The conventional synapses were presumed to arise from ACs; these synapses were annotated, but we did not attempt to identify the presynaptic cells apart from following their processes for a short distance through the volume to ensure that they indeed were ACs (e.g. they lacked presynaptic ribbons and made other conventional synapses). We presume that these conventional synapses are inhibitory, given that most ACs are either GABAergic or glycinergic, but given the existence of at least one type of excitatory AC—the VGLUT3 AC (**Johnson et al., 2004; Kim et al., 2015; Lee et al., 2016**)—it is possible that some subset are excitatory. The VGLUT3 AC itself, however, is unlikely to be a presynaptic partner given that its synaptic inputs and outputs are confined to the central portion of the IPL, whereas the dendrites of the two reconstructed ACs were at the inner and outer margins of the IPL (**Hsiang et al., 2017; Johnson et al., 2004**). Synaptic inputs both from *en passant*, axonal ribbon synapses and from more typical, axon terminal ribbon synapses were observed; analysis of the presynaptic cells revealed them to be ON bipolar cells—both RBs and ON CBs—exclusively, and the synapses therefore are glutamatergic (**Table 2**). Thus, this AC appears to receive only excitatory ON bipolar input despite its being a multi-stratified cell with processes in both ON and OFF sublaminae of the IPL.

The 121 ON CB synapses onto the 2 ACs arose from 67 presynaptic ON CBs, and we skeletonized these ON CBs in order to identify them based on morphological characteristics and axon terminal depth within the IPL (**Figure 4C; Ding et al., 2016; Helmstaedter et al., 2013; Manookin et al., 2008; Sabbah et al., 2017; Stabio et al., 2018**). Most of the presynaptic ON CBs belonged to the type 6 population; the others were a mix of types 5, 7 and 8 CBs (two cells could not be fully reconstructed and were unidentified) (**Figure 4C**). Fifteen *en passant* (axonal) synapses onto the outer (OFF-layer) dendrites of the reconstructed ACs were observed (**Figure 4D**): 13 from type 6 cells and 2 from the unidentified cells (likely type 6 CBs). Both the occurrence of these axonal ON bipolar cell synapses and their general appearance are consistent with previous reports (**Dumitrescu et al., 2009; Hoshi et al., 2009; Kim et al., 2012; Lauritzen et al., 2013**). Additionally, *en passant* synapses in axons of type 6 cells had a markedly distinct appearance from those in the other CB types: for *en passant* synapses in type 6 cells, ribbons tended to occur in clusters of at least three, all apposed to the same postsynaptic process (**Figure 4D; Figure 4—video 1**). In this respect, they resemble

Table 1. Inputs to All amacrine cells.

	All #1	All #2	All #3	Mean ±SD
Inputs (from)				
RB	173	171	176	173 ± 3
AC (Total)	178	177	176	177 ± 1
AC (ON layer)	161 (96%)	157 (89%)	161 (91%)	160 ± 2 (92 ± 4%)
AC (Soma)	17 (4%)	20 (11%)	15 (9%)	17 ± 3 (8 ± 4%)

Table 2. Connectivity of ACs presynaptic to Alls.

	Axons (Figure 3C2)	Cell 1 (Figure 4)	Cell 2 (Figure 4)
Inputs (from)	Total: 2	Total: 314	Total: 297
AC		200 (63.5%)	183 (61%)
RB	1	47 (15%)	56 (19%)
ON CB	1	66 (21%)	55 (18.5%)
Unidentified		2 (<1%)	3 (1%)
Outputs (to)	Total: 1425	Total: 115	Total: 106
All	1212 (85%)	93 (81%)	86 (81%)
RB	173 (12%)	11 (9.5%)	18 (17%)
ON CB	35 (2%)	11 (9.5%)	2 (2%)
Unidentified	5 (<1%)		

strongly the axonal ribbons observed in calbindin-positive ON CBs of the rabbit retina, which are likely homologous to mouse type 6 CBs because both share similar morphology and make synapses with ON α GCs (Hoshi et al., 2009; Kim et al., 2012; Schwartz et al., 2012; Tien et al., 2017). Notably, *en passant* synapses were identified in the axons of some, but not all, reconstructed type 5, 7 and 8 ON CBs, indicating that such synapses are a common feature of ON CBs. None of these synapses, however, were presynaptic to the reconstructed ACs, suggesting that *en passant* synapses are formed with a high degree of target specificity.

The 103 RB synapses with these two ACs arose from 77 RBs (all of which were skeletonized; not shown). All RB→AC synapses were dyads (Figure 4E; Figure 4—video 2); at 75% of these dyads, the AC replaced the A17 (i.e. the other postsynaptic cell was an All), and at the remainder of the dyads, the AC either replaced the All (18%) or else the identity of the second postsynaptic cell could not be confirmed (7%). In at least two of the cases in which the second cell at the dyad could not be identified, the dendrite had the appearance of those of the skeletonized ACs: a very thick dendrite containing clear cytoplasm. Thus, it appears that this AC receives a significant portion of its excitatory input (48%; see Table 2) from the RB population but that any individual RB provides only one or two synapses to a single AC; the latter finding is consistent with the vast majority of RB output being at dyad synapses with All and A17 amacrine cells, in agreement with the standard model of RB synaptic output (Demb and Singer, 2012).

A number of multistratified AC types have been reported in anatomical studies of the mouse retina (Badea and Nathans, 2004; Lin and Masland, 2006; Pérez De Sevilla Müller et al., 2007). The vast majority of these, however, differ in their morphology from the ACs studied here: for example of the 16 wide-field, axon-bearing ACs categorized by Lin and Masland (2006) (their Figure 10), none have axons in the inner (ON) layer of the IPL and a narrow field of dendrites in the outer (OFF) layer. We were struck, though, by the resemblance of the AC identified here to one identified in a screen of Cre-driver lines: the NOS-1 AC of the nNOS-CreER mouse (Zhu et al., 2014). Therefore, we tested the hypothesis that the NOS-1 AC is the spiking, ON AC that provides inhibitory synaptic input to the All.

The NOS-1 AC is a spiking ON cell

NOS-expressing (NOS+) ACs were targeted for *in vitro* recording by crossing nNOS-CreER mice with Cre-dependent reporter mice (Ai32: Chr2/eYFP fusion protein expression; Zhu et al., 2014; Park et al., 2015) and then inducing recombination in ~1 month old offspring by tamoxifen injection (see Materials and methods). eYFP fluorescence (eYFP+) observed by two-photon laser scanning microscopy (2PLSM) was used to target NOS+ ACs for recording. We studied retinas in which Cre expression was induced robustly; these had 110 ± 5 cells mm^{-2} (mean \pm SEM) labeled in the GCL and 128 ± 5 cells mm^{-2} labeled in the INL ($n = 7$ retinas from 7 mice). Based on an earlier description of this driver line, we assumed that labeled cells in the GCL included a mixture of NOS-1 and NOS-2 ACs, with NOS-1 cells having the bistratified morphology described here and NOS-2 cells exhibiting thick, spiny dendrites that project into the central level of the IPL, between the layers marked by

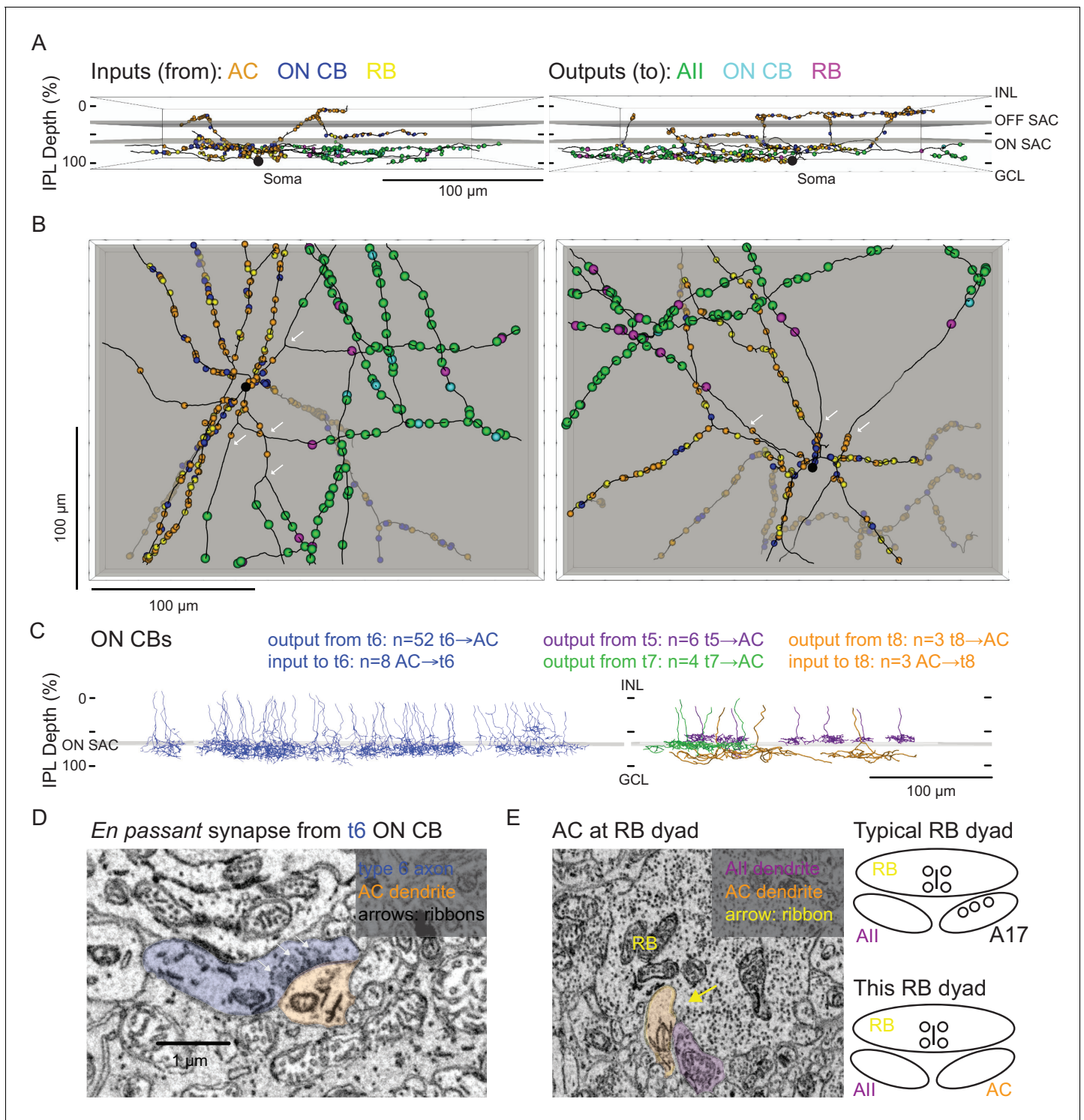


Figure 4. Anatomical characterization of an AC presynaptic to the AII. (A) Skeletonization and annotation of two ACs (left and right panels) with similar morphologies and patterns of synaptic connectivity. Note that both cells, viewed from the side, as in a transverse section through the retina, have similar neurite branching patterns and receive synaptic input from ACs and from ON CBs on dendrites in the OFF laminae of the IPL, on the outer side of the OFF SAC dendrites (i.e. close to 0% IPL depth; here, SAC dendrites are represented as gray rectangles). AC dendrites and annotations are contained within **Source data 1** and downloadable in Knossos XML format. (B) An *en face* view (viewed from the GCL; the gray represents the layer of ON SAC dendrites) of the two ACs illustrated in (A). Note that their synaptic inputs and outputs are segregated to different sections of their processes; the area receiving input is dendritic, and the area making output is axonal. White arrows indicate areas where dendrites become axons (inputs are proximal to the arrow, closest to the soma; outputs are distal to the arrow, farther from the soma). AC skeletons and annotations are contained within *Figure 4 continued on next page*

Figure 4 continued

Source data 1 and downloadable in Knossos XML format. (C) Side (transverse) view illustrating all ON CBs pre- or postsynaptic to the two ACs illustrated in (A) and (B). ON CBs were classified based on axon branching pattern and stratification depth relative to the ON SAC dendrites (Helmstaedter et al., 2013). CB skeletons and annotations are contained within **Source data 2** and downloadable in Knossos XML format. (D) Example *en passant* ribbon-type synapses in a type 6 ON CB axon. Note three ribbons clustered together and presynaptic to the same AC process. See **Figure 4—video 1** for a larger image stack. (E) Example of RB dyad at which the AC type shown in (A) and (B) replaces the A17 as one of the two postsynaptic cells (see schematic at right). See **Figure 4—video 2** for a larger image stack.

The online version of this article includes the following video(s) for figure 4:

Figure 4—video 1. Image stack containing *en passant* type 6 CB→AC synapses illustrated in **Figure 4D**.

<https://elifesciences.org/articles/56077#fig4video1>

Figure 4—video 2. Image stack containing RB→All, AC dyad synapse illustrated in **Figure 4E**.

<https://elifesciences.org/articles/56077#fig4video2>

dendrites of ON and OFF starburst ACs (Jacoby et al., 2018; Zhu et al., 2014). Labeled cells in the INL included additional NOS-2 ACs (Zhu et al., 2014) as well as other AC types that projected into the outer most levels of the IPL but were not studied here.

Dye filling (Lucifer Yellow) of recorded eYFP⁺ cells in the GCL revealed that these cells most typically were NOS-1 ACs, with bistratified dendrites and long axons in the ON sublaminae identified by 2PLSM visualization following recording and, in some cases, by subsequent analysis by confocal microscopy ($n = 13$ cells; **Figure 5A**). All spiking cells that were imaged shared a similar morphology, indicating that they represent a single cell type (Zhu et al., 2014). We examined NOS-1 light responses using contrast modulation around a bright mean luminance ($10^4 R^* \text{ cone}^{-1} \text{ s}^{-1}$), because the IR laser exposure used to identify fluorescent cells in 2PLSM partially bleaches rods (see Borghuis et al., 2013; Borghuis et al., 2011). Under this condition, whole-cell recordings of membrane voltage (i.e. current-clamp recordings) showed that NOS-1 cells fired spikes in response to positive contrast and that spiking could be suppressed completely by negative contrast (**Figure 5B**). Responses increased in magnitude with increasing spot diameter, suggesting an integration area of at least $\sim 500 \mu\text{m}$ diameter (**Figure 5C**).

NOS-2 cell membrane voltage responses to light clearly differed from those of NOS-1 cells (**Figure 5D,E**). NOS-2 cells were non-spiking with graded, depolarizing responses to both positive and negative contrast and are therefore ON-OFF cells (Jacoby et al., 2018). Both ON and OFF responses of NOS-2 cells increased with spot diameter, with a relatively more gradual increase for the OFF response (**Figure 5F**).

Voltage-clamp recording from NOS-1 cells demonstrated that positive contrast evoked excitatory synaptic input, measured as inward current relative to a baseline holding current ($V_{\text{hold}} = E_{\text{Cl}}$) (**Figure 5G,H**). Negative contrast evoked a reduction of this baseline holding current, consistent with temporary suppression of ongoing presynaptic glutamate release (**Figure 5G,H,I**). Excitatory input was blocked completely by L-AP4, which suppresses the responses of ON bipolar cells, and therefore, excitation was mediated exclusively by the ON pathway (Slaughter and Miller, 1981; **Figure 5G**). Inhibitory synaptic input ($V_{\text{hold}} = E_{\text{cat}}$) was measured at both positive and negative contrast, but the amplitude of the modulated current typically was small under control conditions. In the presence of L-AP4, however, inhibition persisted only in response to negative contrast and, indeed, increased by $38 \pm 11.4 \text{ pA}$ in amplitude ($t = 3.3$; $n = 9$; $p < 0.005$; **Figure 5G–I**). This increase could reflect relief of ON pathway-mediated suppression of inhibitory input from OFF ACs to NOS-1 ACs. In summary, though, these experiments demonstrate conclusively that NOS-1 cells receive tonic glutamatergic input from ON bipolar cells that can be modulated by contrast as well as inhibitory inputs from ACs in both ON and OFF pathways.

The NOS-1 AC is the predominant NOS-expressing AC in the ganglion cell layer and is distinct from CRH-expressing ACs

To determine the relative density of displaced NOS-1 and NOS-2 ACs in the GCL of the nNOS-CreER retina, we made loose patch recordings of responses to light from displaced eYFP⁺ ACs targeted by 2PLSM (**Figure 6A**). Most displaced ACs were spiking cells with sustained ON responses, confirming their identity as NOS-1 cells ($n = 22/26$ cells, three retinas from two mice). One exception was a spiking cell with both ON and OFF responses (**Figure 6A**, asterisk); we did not study this cell

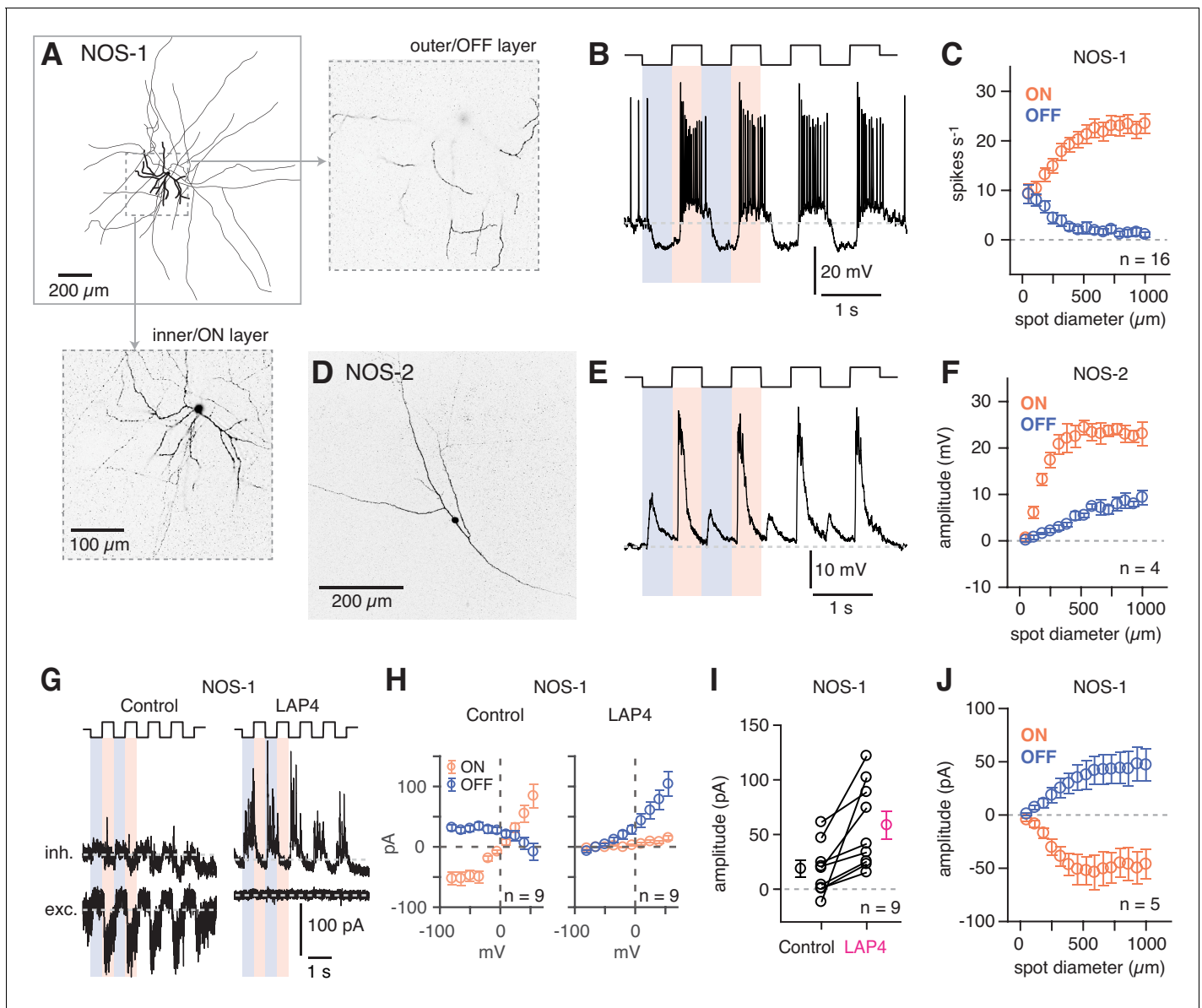


Figure 5. NOS-1 ACs are spiking ON-center cells that can be distinguished from NOS-2 ACs. (A) Morphology of a NOS-1 AC. Dendrites (thick) and axons (thin) were drawn from confocal images of a NOS-1 AC filled by Lucifer Yellow during whole-cell recording. Single confocal sections are shown for the inner/ON and outer/OFF layers of processes for the region indicated (dashed, boxed region). The cell is bistratified in the region proximal to the cell body; only the ON-layer processes are shown in the drawing. (B) Membrane potential recording for the cell in (A). The cell had a baseline firing rate at mean luminance ($\sim 10^4 R^*/\text{cone/s}$) that modulated above and below baseline during positive and negative contrast periods, respectively (spot diameter, 600 μm ; 100% contrast). (C) Population ($n = 16$ cells) changes in firing rate during positive contrast (ON response) and negative contrast (OFF response) as a function of spot size (100% contrast). Firing rate was computed over a 500 ms time window for each contrast. Error bars indicated \pm SEM across cells. (D) Collapsed confocal stack (maximum projection image) of a filled NOS-2 cell. (E) The NOS-2 cell in (D) responds with depolarization at both positive and negative contrast, an ON-OFF response (spot diameter, 600 μm ; 100% contrast). (F) Population ($n = 4$ cells) changes in membrane potential as a function of spot size (measured over a 100 ms time window). Conventions are the same as in (C). (G) Excitatory and inhibitory current measured in a NOS-1 cell to a spot stimulus (diameter, 400 μm). After adding L-AP4 (20 μM) to suppress the ON pathway, the excitatory current is blocked and the inhibitory current increases and is OFF responding. (H) Current-voltage (I-V) plots for ON and OFF responses for data in (G) averaged across cells (measured over a 100- to 200-ms time window). Error bars indicate \pm SEM across cells. (I) Population change in the OFF inhibitory current after adding L-AP4. Individual cell data are connected by lines. Population data indicate mean \pm SEM across cells. (J) Excitatory current amplitude for a population of NOS-1 cells ($n = 5$ cells) as a function of spot diameter (100% contrast; measured over a 100 ms time window). Error bars indicate \pm SEM across cells.

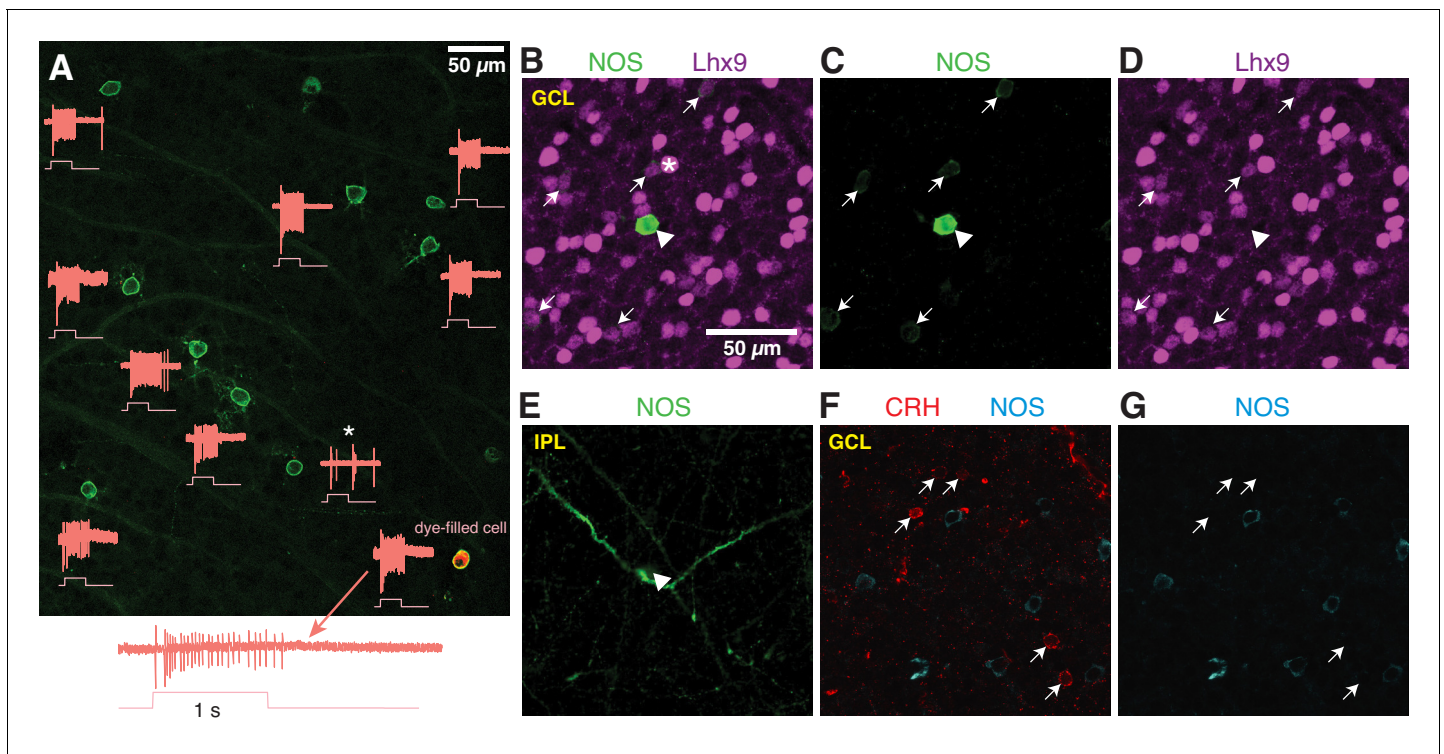


Figure 6. NOS-expressing ACs in the ganglion cell layer are primarily NOS-1 cells. (A) Loose-patch spike recording from a region of retina with cells labeled in the nNOS-CreER x Ai32 mouse. The response to a light flash (800- μ m diameter, $\sim 10^4$ R*/cone/s) is shown next to each soma that was recorded. The majority of cells showed a sustained ON response in the spike rate during the light flash. In one case, the response differed (*) and showed a transient ON-OFF response. The cell at lower right was subsequently studied by whole-cell recording and was filled with dye; for this cell, the spike response is shown at an expanded scale below the image. (B–E) P12 retinas (C57/B6 wild-type) stained with antibodies to label NOS and Lhx9 expressing cells in the GCL. Most NOS-expressing cells showed dim labeling for Lhx9 antibody (arrows). A well-stained NOS-expressing cell in the center (arrow-head) did not show Lhx9 labeling. Laser power was increased for Lhx9 imaging, such that fluorescence of strongly-labeled cells was saturated (*, example cell), making it easier to visualize weakly-labeled cells. NOS labeling alone (C) and Lhx9 labeling alone (D). (E) Same as (C) with the image plane shifted to the inner plexiform layer (IPL). The NOS-expressing cell that lacked Lhx9 expression (arrowhead) had thick dendrites that could be followed into the IPL, with the characteristic properties and stratification of a NOS-2 cell. (F–G) P12 retina (C57/B6) stained with antibodies to label corticotropin releasing hormone (CRH) and NOS. NOS-expressing cells do not overlap with CRH-expressing cells. NOS labeling alone (G). Scale bar in (B) applies to (B) – (G).

further, but it likely represents either a subtype of nNOS AC that is primarily in the INL and only rarely displaced to the GC or a case of ectopic Cre and/or reporter expression. In the NOS-1 population, ~ 2 – 3 cells could typically be found within $\sim 54,500 \mu\text{m}^2$, the cross-sectional area of our SBEM volume; this cell density is consistent with our finding two putative NOS-1 cells in the SBEM data set.

Additionally, we examined NOS-expressing cells by nNOS antibody labeling during a developmental period (P8 – P14) during which a subset of NOS+ cells express the transcription factor Lhx9 (Balasubramanian et al., 2018). Two populations of NOS+ cells were observed: a small group of brightly-labeled cells ($n = 19$ cells) and a much larger group of dimly-labeled cells ($n = 550$ cells; six retinas from six mice; $n = 2$ retinas each at P8, P12 and P14). In retinas double-labeled with the Lhx9 antibody (two retinas from two animals, P12), only the dimly-labeled NOS+ cells were Lhx9+ (Figure 6B–D) ($n = 146/156$ cells). The brightly-labeled, Lhx9- cells ($n = 5/5$ cells, two retinas from two mice) exhibited dendrites that could be followed into the center of the IPL, where they gave rise to the thick, spiny processes characteristic of NOS-2 cells (Figure 6E). We conclude that Lhx9 expression distinguishes presumptive NOS-1 from NOS-2 cells in the GCL at P12, and that at all developmental time points, NOS-2 cells are rarely found in the GCL (3.3% of cells), making NOS-1 cells a large majority in the GCL (96.7% of NOS+ cells).

The NOS-1 cell was described also as the CRH-2 AC (Corticotropin-releasing hormone AC-2) based on labeling in the CRH-ires-Cre retina (Zhu *et al.*, 2014). We, however, found that Cre-expressing cells in the CRH-ires-Cre::Ai32 retina are rarely labeled by the nNOS antibody (Park *et al.*, 2018), suggesting limited overlap in CRH+ and NOS+ AC populations. Indeed, we found no co-expression of CRH and NOS by immunohistochemistry (P12 retina) ($n = 66$ CRH+ cells and 85 NOS+ cells, one retina) in neurons in the GCL (Figure 6E–G). Thus, NOS-1 ACs do not appear to co-express CRH, and we conclude, then, that Cre expression in NOS-1 ACs of the CRH-ires-Cre line is rare and unsystematic.

Confirmation of synapses between NOS-1 cells and Alls

To demonstrate that NOS-1 ACs provide synaptic input to Alls, we eliminated Cre-expressing ACs in the nNOS-CreER retina by intraocular injection of an AAV containing a Cre dependent-DTA construct followed 2–3 days later by tamoxifen administration. Four weeks later, we stimulated the retina in vitro with dim (40 R*/rod/s) spots of varying size and recorded light-evoked currents in Alls at $V_{\text{hold}} = E_{\text{Cl}}$ or $V_{\text{hold}} = E_{\text{cat}}$ (Figure 7A; as in Figure 2A). Following ablation of NOS+ ACs (including both NOS-1 and NOS-2 cells), the recorded excitatory currents were smaller than in the control condition and were unaffected by TTX (Figure 7B,C; compare to Figure 2B), consistent with a loss of inhibitory input from NOS-1 ACs to presynaptic RBs (Figure 4 and Table 2). Most significantly, though, we observed a lack of inhibitory TTX-sensitive surround in All responses following NOS+ AC ablation (Figure 7B,D): the TTX-sensitive IPSCs evoked by large-diameter spots (590 to 800 μm) were significantly smaller in DTA-expressing retinas than in control mice that received the same AAV and tamoxifen injections but were Cre-negative.

We confirmed the elimination of NOS+ ACs by nNOS antibody staining and found that the number of NOS+ cells was reduced strongly in DTA-expressing retinas relative to controls (Figure 7E,G). To confirm that DTA expression did not result in non-specific ablation of ACs, we used ChAT antibody immunolabeling to quantify the number of starburst ACs (in both the INL and GCL) in control and DTA-expressing retinas and found no reduction in the experimental group (Figure 7F,H). Thus, elimination of NOS+ ACs provides evidence that a NOS+ cell, most likely the NOS-1 AC, is necessary for generating the All inhibitory surround.

To confirm that NOS-1 ACs provide synaptic input to Alls, we performed optogenetic circuit-mapping experiments after inducing Chr2/eYFP expression in NOS+ cells, as described above. After blocking the influence of the photoreceptors (see Materials and methods), we recorded from cells in a retinal whole-mount preparation and stimulated Chr2-expressing neurons with bright blue light. A representative Chr2-expressing NOS-1 cell ($n = 3$ total) responded within a few ms of the optogenetic stimulus with increased spiking (Figure 8A); IPSCs recorded in Alls (normalized to their peak amplitude, 39 ± 6 pA) were observed a few ms later (Figure 8A), consistent with a monosynaptic connection from NOS-1 cells.

Chr2-evoked IPSCs in Alls were blocked by SR95531 (50 μM) and therefore were mediated by GABA_A receptors (Figure 8B,C) (reduction of 34.5 ± 11.7 pA, or $108 \pm 4\%$; $t = 28.5$; $n = 4$; $p < 0.001$). In a second group of cells, the IPSCs were blocked by TTX (1 μM), indicating that they arose from a spiking presynaptic AC (Figure 8D,E) (reduction of 35.1 ± 8.9 pA or $105 \pm 4\%$; $t = 29.5$; $n = 5$; $p < 0.001$). These results are consistent with a direct synaptic input from the NOS-1 AC to the All because input from the non-spiking NOS-2 AC would not be TTX-sensitive. The spiking dopaminergic AC (DAC) also makes GABAergic synapses with the somas and proximal dendrites of Alls (Figures 3B2, C3–5) (Gustincich *et al.*, 1997), but the DACs in the nNOS-CreER retina do not express Chr2/eYFP, as demonstrated immunohistochemically: there was no overlap between TH+ cells, identified by TH immunolabeling ($n = 90$ cells), and eYFP+ cells ($n = 198$ cells, five retinas from three mice) (Figure 8F,G).

Additionally, we recorded Chr2-evoked IPSCs in RBs in retinal slices ($n = 2$) to confirm the functionality of NOS-1 AC→RB synapses observed in our anatomical analyses (Figures 3C1, C2, C6 and 4A,B). Here, we had to include the K channel blockers 4-AP (1 μM) and TEA (10 μM) in the external solution to enhance the excitability of cut NOS-1 AC axons so that they could be stimulated adequately in the slice (Figure 9, left). Indeed, control experiments recording from Alls in both slice (Figure 9, left) and whole-mount (Figure 9, right) retinal preparations demonstrated that this manipulation enhanced release from NOS-1 cells significantly ($n = 3$); IPSCs were blocked by picrotoxin (50

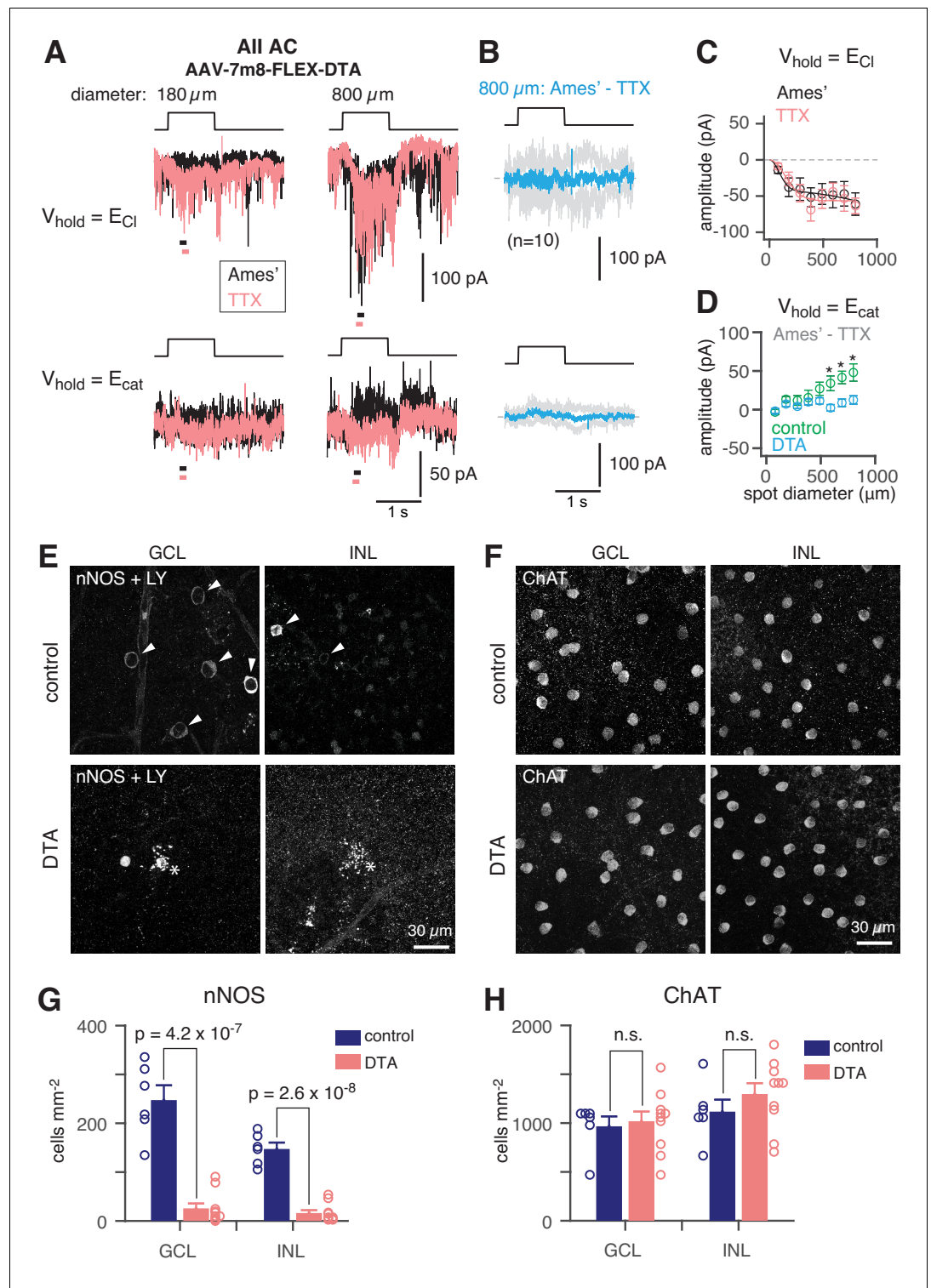


Figure 7. NOS+ ACs generate the TTX-sensitive receptive field surround of the All. (A) All responses to spots (diameter indicated; 40 R*/rod/s, 1 s duration) in control (Ames') and in TTX (1 μM) recorded at E_{Cl} (-70 mV; top) and near E_{cat} ($+5$ mV; bottom) in a nNOS-CreER retina injected with Cre-dependent DTA virus (AAV-7m8-FLEX-DTA). (B) Difference current at each V_{hold} for the 800 μm diameter spot (average of $n = 10$ cells; shaded areas are \pm SEM across cells as a function of time). (C) Spot (variable diameter) response amplitudes [measured over a 150 ms time window, indicated by horizontal bars in A] at $V_{\text{hold}} = E_{\text{Cl}}$ ($n = 10$ cells). Error bars are \pm SEM across cells. (D) Difference current amplitude at $V_{\text{hold}} = E_{\text{cat}}$ averaged across cells. Same conventions as in (C). Recordings
Figure 7 continued on next page

Figure 7 continued

from control retinas are superimposed ($n = 6$ cells). Control mice had the same AAV and tamoxifen injections but were Cre-negative. Responses were smaller in the DTA group compared to the control group (one-tailed t-tests, *): $590 \mu\text{m}$, $t = 3.16$, $p = 3.51 \times 10^{-3}$; $695 \mu\text{m}$, $t = 3.31$, $p = 2.12 \times 10^{-3}$; $800 \mu\text{m}$, $t = 2.93$, $p = 5.45 \times 10^{-3}$). (E) nNOS immunolabeling in GCL and INL, centered on a region with a recorded All (visible in some images, marked by *). (F) Same format as (E) for ChAT immunolabeling of starburst ACs. (G) NOS+ cell density over a square region (0.64×0.64 mm) centered on a recorded All and visualized by nNOS immunolabeling: DTA ($n = 10$ retinas) vs. control ($n = 6$ retinas). Virus-injected retinas had significantly fewer cells (one-tailed t-test): GCL, $t = 8.35$, $p = 4.2 \times 10^{-7}$; INL, $t = 10.5$, $p = 2.6 \times 10^{-8}$. (H) Same format as (G) for ChAT immunolabeling. Cell density assessed over a square region (0.16×0.16 mm) centered on a recorded All. Starburst AC density in DTA virus-injected retinas ($n = 10$) was not significantly (n.s.) different than in control retinas ($n = 6$): GCL, $t = -0.35$; INL, $t = -1.05$.

μM). Notably, enhancing excitability in both retinal slices and whole-mount preparations did not change the latency of the IPSCs, supporting the conclusion that they are monosynaptic.

Discussion

Here, we investigated an unresolved mechanism for the inhibitory, receptive field surround of the central interneuron in the RB pathway, the All AC (**Figure 1**). Ultrastructural analysis of inhibitory input to three Alls indicated that the majority of AC synapses arise from a single type of displaced, multistratified, wide-field cell that contacts Alls preferentially. Two relatively complete examples of this AC were found within our SBEM volume, and examination of this cell type's outputs revealed that ~80% of its synapses were presynaptic to Alls, with the majority of the remainder presynaptic to RBs. This AC received excitatory input exclusively from ON bipolar cells, both at *en-passant* axonal synapses in the OFF strata of the IPL and at axon terminal synapses in the ON strata of the IPL. The AC identified by SBEM analysis is a morphological match to the genetically identified NOS-1 AC, which we demonstrated to have physiological functions predicted by the ultrastructural analysis: it is an ON AC that provides GABAergic inhibition to Alls and RBs. We therefore consider the NOS-1 AC to be an integral part of the well-studied mammalian RB pathway, serving as the major source of direct, long-range inhibition during night vision.

Multiple cell types in nNOS-creER retina

Cre-mediated recombination drove ChR2/eYFP reporter expression in multiple AC types in the nNOS-creER retina. We observed two AC types, called NOS-1 and NOS-2, (**Jacoby et al., 2018; Zhu et al., 2014**), consistent with reports of nNOS expression in at least two AC types (**Chun et al., 1999; Kim et al., 1999**).

The NOS-1 AC is described above. The NOS-2 AC is a monostratified cell, with dendrites in the center of the IPL (between the processes of ON and OFF starburst ACs; **Figure 5D**); its soma is either in the conventional location in the INL (~75%) or displaced to the GCL (~25%) (**Chun et al., 1999; Jacoby et al., 2018; Kim et al., 1999; Zhu et al., 2014**). There were additional labeled ACs in the INL of the nNOS-CreER retina: their processes stratified in the OFF layers proximal to the INL, but the cells were not characterized further.

Our anatomical evidence, however, supports the conclusion that the NOS-1 AC is the only Cre-expressing AC presynaptic to the All: NOS-2 dendrites are confined to the center of the IPL, between the OFF and ON starburst ACs, whereas inhibitory inputs to Alls are either distal to the OFF starburst processes and apparently arise from dopaminergic ACs (not labeled in the nNOS-CreER line; **Figure 6F,G**) or proximal to the ON starburst AC processes (**Figure 3**). As well, in tracing many AC inputs to Alls, composing ~25% of the total inhibitory synaptic input to these Alls, we never encountered an axon that stratified between the ON and OFF starburst ACs.

The NOS-1 AC is the dominant inhibitory input to the All and generates the All surround

The All has an ON-center receptive field with an antagonistic surround (**Bloomfield and Xin, 2000; Nelson, 1982; Xin and Bloomfield, 1999**). The surround is mediated by GABAergic inhibition, it depends on activation of ON bipolar cells, and it is blocked by TTX, indicating that it arises from a

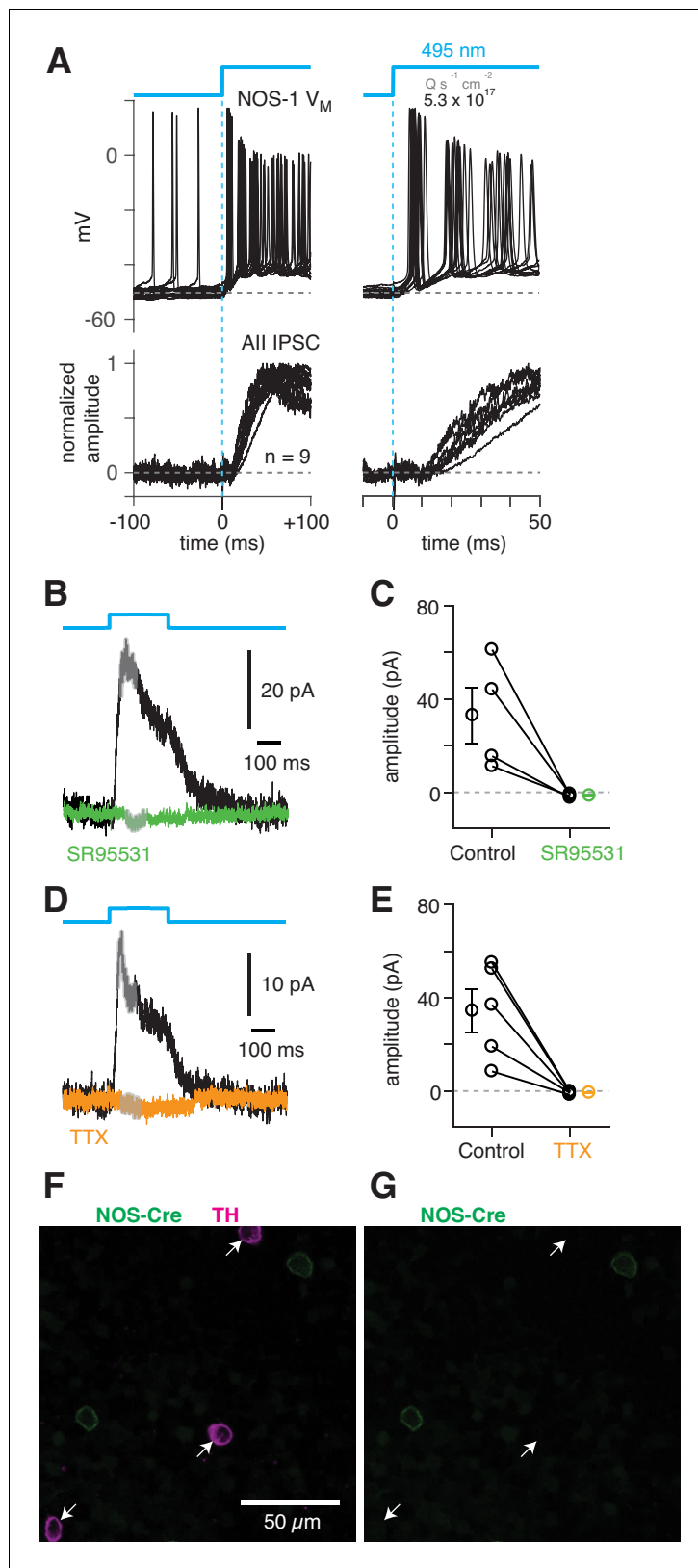


Figure 8. NOS-1 cells make synapses with All amacrine cells. (A) Top/Left, optogenetic stimulation of a Chr2-expressing NOS-1 cell (of n = 3 total) in the nNOS-CreER::Ai32 retina responded with increased spike firing to blue light (n = 12 trials overlaid). Response was recorded in whole-mount retina in the presence of drugs to block Figure 8 continued on next page

Figure 8 continued

photoreceptor-mediated inputs to retinal circuitry: DNOX (50 μ M), D-AP5 (50 μ M), L-AP4 (2 μ M), and ACET (1 μ M). Bottom/Left, the optogenetic stimulus evoked IPSCs ($V_{\text{hold}} = E_{\text{cat}}$) in All ACs ($n = 9$ cells). Responses are normalized to the maximum amplitude, 39 ± 6 pA (measured over a 60–70 ms time window). Right, expanded version of traces at left. The initial spike in the NOS-1 cell occurred a few milliseconds after optogenetic stimulation (top), followed a few milliseconds later by the onset of IPSCs in the All. (B) In All ACs recorded under the conditions in (A), inhibitory current (measured over the gray region) was blocked by the GABA-A receptor antagonist SR95531 (50 μ M). (C) Effect of SR95531 in a sample of All ACs ($n = 4$ cells). Error bars indicate \pm SEM across cells. (D) Same format as (B) with the sodium channel blocker TTX (1 μ M). (E) Same format as (C) with TTX ($n = 5$ cells). (F) Confocal image of the inner nuclear layer of a retina from the nNOS-creER::Ai32 mouse. A tyrosine-hydroxylase (TH) antibody was used to label dopaminergic ACs (arrows), which did not overlap with Cre-expressing NOS+ ACs. (G) Same image as (F) without the TH labeling. None of the cells with TH immunolabeling (arrows) were eYFP+.

spiking AC (Bloomfield and Xin, 2000; Figure 2D–G). The NOS-1 AC satisfies all of the criteria for the mechanism generating the All surround: it is a GABAergic (Figure 8A,B; Zhu et al., 2014), spiking ON AC (Figure 5B,C; Figure 8C,D; Jacoby et al., 2018) that provides the majority of its synaptic output to Alls (Figures 3 and 4; Table 2). Furthermore, NOS+ ACs are necessary for generating TTX-dependent surround inhibition in Alls (Figure 7A,B).

Our conclusion that the NOS-1 AC provides ~90% (Table 1) of the inhibitory input to the All is based on the assumption—strongly supported by the anatomical evidence (Figures 3 and 4)—that a single cell type is presynaptic to all of the inhibitory synapses on the distal dendrites of Alls. Given that every inhibitory input to the distal dendrites of three Alls analyzed arises from a process with a stereotyped pattern of synaptic output (Figures 3C2 and 4A,B), we assume they represent a single type. The alternative seems very unlikely: that there are multiple independent populations of amacrine cell, each of which has axons identical in appearance, running in exactly the same stratum of the IPL, providing the identical pattern of 80% output to Alls and 20% output to RBs, and matching precisely the pattern of output of the two reconstructed cells (both of which share identical patterns of inputs as well as outputs). Indeed, it is established that individual retinal neuron types are defined by their highly stereotyped patterns of connectivity (Briggman et al., 2011; Cohen and Sterling, 1990; Graydon et al., 2018; Hoggarth et al., 2015). Further, the combination of wide-field axons in the ON laminae of the IPL and narrow-field dendrites in the OFF laminae of the IPL apparently is restricted to a single population of wide-field AC (Lin and Masland, 2006; Zhu et al., 2014). Finally, transcriptomic analysis supports the existence of two strongly expressing NOS+ ACs: NOS-1 and NOS-2 (Yan et al., 2020).

From our SBEM analysis, the multi-stratified AC presynaptic to the All is predicted to be an ON cell that should be activated by dim scotopic stimuli owing to its input from RBs as well as from type 6 CBs, which are well-coupled to the All network (Grimes et al., 2014b): our observations of the light responses of NOS-1 ACs (Figure 6), their synaptic connectivity (Figures 8–9), and the properties of surround suppression of GC responses to dim light stimuli (Figure 2D) collectively support the conclusion that the NOS-1 AC is the primary inhibitory neuron influencing the output of the All network to rod-driven input. As well, it is notable that the NOS-

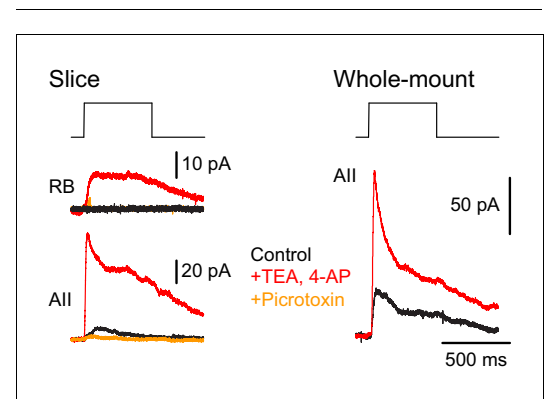


Figure 9. NOS-1 ACs make synapses with RBs. At left, recordings from a RB (top) and an All (bottom) in a retinal slice demonstrate that optogenetic stimulation of cre-expressing cells in the nNOS-CreER::Ai32 retina evoked inhibitory currents ($V_{\text{hold}} = E_{\text{cat}}$). Potentiation of presynaptic depolarization with K channel blockers was necessary to elicit responses in RBs owing to the small number of presynaptic axons preserved in the 200 μ m thin slice. At right, K channel blockers potentiate larger inhibitory currents ($V_{\text{hold}} = E_{\text{cat}}$) recorded in an All and evoked by optogenetic stimulation of cre-expressing cells in a whole-mount preparation of nNOS-CreER::Ai32 retina.

1 AC appears to be one significant mechanism by which cone pathways can inhibit rod pathways (Lauritzen *et al.*, 2019). And, given that the NOS-1 AC produces NO, which is thought to regulate electrical transmission between Alls and ON cone bipolar cells (Mills and Massey, 1995), it is possible that synaptic inhibition of the All is coupled with modulation of its electrical synapses. As noted above, we did not measure directly the NOS-1 AC response threshold to dim light due to the laser exposure required for cell targeting, but the response threshold of the NOS-1 AC is presumably among the most sensitive in the retina due to its input from RBs and type 6 CBs.

Functional relevance

As luminance increases from visual threshold to 10–20 R*/rod/s, the gain of transmission at the RB→All synapse is reduced (Dunn *et al.*, 2006; Dunn and Rieke, 2008), and Alls hyperpolarize; this hyperpolarization spreads to the terminals of type 6 CBs, which increases rectification while relieving activity-dependent synaptic depression at type 6→ON α GC synapses (Grimes *et al.*, 2014a). The hyperpolarization of the All in background light has been attributed to synaptic depression at the RB→All synapse (Grimes *et al.*, 2014a), but this hyperpolarization likely also depends on direct synaptic inhibition from the NOS-1 AC. The combined influence of these synaptic mechanisms would allow the RB pathway to remain functional at backgrounds as high as 250 R*/rod/s (Ke *et al.*, 2014).

Thus, inhibitory input from the NOS-1 AC might represent a significant modulatory mechanism within the RB pathway and could be responsible for maintaining high-fidelity signaling through a range of background luminance at which differentiating signal from noise is a particular concern. More generally, because the type 6 CB provides input to the NOS-1 AC and is coupled electrically to the All network that is inhibited by the NOS-1 AC, we propose that a type 6 CB→NOS-1 AC→All AC→type 6 CB feedback circuit could maintain the rectifying nature of transmission at type 6 CB synapses by preventing excessive presynaptic depolarization across a range of lighting conditions. Testing this prediction would require the inactivation or ablation of NOS-1 cells while recording at various stages of the RB pathway. A limitation of the nNOS-CreER retina is that Cre is expressed in several cell types, including the NOS-2 cell, which is the main source of NO release within the retina (Jacoby *et al.*, 2018). Improvements in the selective targeting of NOS-1 cells will be an important step in evaluating its function in retinal circuitry and behavior.

Conclusion

We uncovered the dominant inhibitory input to the All, the central neuron in the well-studied RB pathway of the mammalian retina. The NOS-1 AC is the spiking neuron responsible for generating the TTX-sensitive, GABAergic surround that modulates All network function across a range of lighting conditions (Bloomfield and Xin, 2000; Xin and Bloomfield, 1999). Further, our anatomical analysis also explained the ON response of a multi-stratified AC with neurites and excitatory synaptic inputs in both the ON and OFF strata of the IPL. Our study thereby extends the classification of retinal neurons that receive ON input from *en-passant* axonal synapses made by ON bipolar cells in the OFF strata of the IPL, which also includes the dopaminergic AC and the intrinsically photosensitive ganglion cells (Dumitrescu *et al.*, 2009; Hoshi *et al.*, 2009; Sabbah *et al.*, 2017). Our study demonstrates the utility of a targeted connectomic analysis coupled with neurophysiological investigation to neural circuit discovery.

Materials and methods

Key resources table

Reagent type (species) or resource	Designation	Source or reference	Identifiers	Additional information
Genetic reagent (<i>Mus musculus</i>)	C57BL/6J	Jackson Laboratory Stock #000664	IMSR Cat# JAX000664, RRID:IMSR_JAX:000664	Wild type mouse
Genetic reagent (<i>M. musculus</i>)	nNOS-CreER	Jackson Laboratory Stock #014541	IMSR Cat# JAX014541, RRID:IMSR_JAX:014541	Transgenic mouse: cre-driver line

Continued on next page

Continued

Reagent type (species) or resource	Designation	Source or reference	Identifiers	Additional information
Genetic reagent (<i>M. musculus</i>)	Ai14	Jackson Laboratory Stock #007914	IMSR Cat# JAX007914 RRID:IMSR_JAX:007914	Transgenic mouse: cre-dependent tdTomato expression
Genetic reagent (<i>M. musculus</i>)	Ai32	Jackson Laboratory Stock #024109	IMSR Cat# JAX024109 RRID:IMSR_JAX:024109	Transgenic mouse: cre-dependent ChR2/eYFP expression
Recombinant DNA reagent	AAV2/7m8-CAG-FLEX-DTA-WPRE-SC40pA	This paper		Adeno-associated virus; 10 ¹³ GC/ml
Recombinant DNA reagent	pAAV-Syn-FLEX-rc[CoChR-GFP]	PMID:24509633	Addgene #62724; RRID:Addgene_62724	Plasmid
Recombinant DNA reagent	pAAV-CAG-fDIO-oG-WPRE-SV40pA	PMID:27149846	Addgene #74291; RRID:Addgene_74291	Plasmid
Recombinant DNA reagent	PGKdtabpA	PMID:9226440	Addgene #13440; RRID:Addgene_13440	Plasmid
Recombinant DNA reagent	AAV2/7m8 capsid	Gift of Dr. John Flannery, UC Berkeley; PMID:23761039	Addgene #64839; RRID:Addgene_64839	Plasmid
Antibody	anti-ChAT (Goat polyclonal)	EMD Millipore	Cat# AB144P; RRID:AB_2079751	1:200 dilution
Antibody	anti-LuciferYellow (Rabbit polyclonal)	ThermoFisher Scientific	Cat# A-5750; RRID:AB_2536190	1:2000 dilution
Antibody	anti-nNOS (Rabbit polyclonal)	ThermoFisher Scientific	Cat# 61-7000; RRID:AB_2313734	1:500 dilution
Antibody	anti-nNOS (Guinea pig polyclonal)	Frontier Institute	Cat# Af740; RRID:AB_2571816	1:2000 dilution
Antibody	anti-TH (Rabbit polyclonal)	EMD Millipore	Cat# AB152; RRID:AB_390204	1:1000 dilution
Antibody	anti-human/rat CRF serum (Rabbit polyclonal)	gift of Dr. Paul Sawchenko, Salk Institute	Code# PBL rC68	1:40,000 dilution
Antibody	anti-LHX9 (Guinea pig polyclonal)	gift of Dr. Jane Dodd, Columbia University		1:20,000 dilution
Antibody	Donkey Anti-Goat AlexaFluor 633 secondary	ThermoFisher Scientific	Cat # A-21082; RRID:AB_2535739	1:500 dilution
Antibody	Donkey Anti-Rabbit AlexaFluor 488 secondary	Jackson ImmunoResearch	Cat# 711-545-152; RRID:AB_2313584	1:500 dilution
Antibody	Donkey Anti-Rabbit Cy3 secondary	Jackson ImmunoResearch	Cat# 711-165-152; RRID:AB_2307443	1:500 dilution
Antibody	Donkey Anti-Rabbit Cy5 secondary	Jackson ImmunoResearch	Cat# 711-175-152; RRID:AB_2340607	1:500 dilution
Antibody	Donkey Anti-Guinea pig secondary	Jackson ImmunoResearch	Cat# 706-175-148; RRID:AB_2340462	1:500 dilution
Software, algorithm	ScanImage	http://scanimage.vidriotechnologies.com/ PMID:12801419	RRID:SCR_014307	Software for 2PLSM

Continued on next page

Continued

Reagent type (species) or resource	Designation	Source or reference	Identifiers	Additional information
Software, algorithm	ParaView	https://www.paraview.org/	RRID:SCR_002516	Software for visualization
Software, algorithm	IgorPro	https://www.wavemetrics.com/	RRID:SCR_000325	Software for data acquisition and analysis
Software, algorithm	PClamp	https://www.moleculardevices.com/	RRID:SCR_011323	Software for data acquisition and analysis
Software, algorithm	Knossos	https://knossos.app/ PMID:21743472	RRID:SCR_003582	Software for volumetric imaging analysis
Software, algorithm	ImageJ	https://ImageJ.net	RRID:SCR_003070	Software for cell counting and image projection

TEM

An excised retina was fixed for one hour at room temperature with 2% glutaraldehyde in 0.15 M cacodylate buffer, washed in three changes of the same buffer, and postfixed with 1% osmium tetroxide in 0.15 M cacodylate containing 1.5% potassium ferrocyanide. A wash in three changes of distilled water followed the reduced osmium fixation and preceded an *en bloc* fix in 2% aqueous uranyl acetate. Dehydration in a graded series of ethanol (35% to 100%), and infiltration in a propylene oxide:epoxy resin series was followed by embedding and polymerization in epoxy resin. Thin sections were cut on a Reichert Ultracut E ultramicrotome, stained with 2% uranyl acetate and 0.2% lead citrate before being viewed and photographed on a Zeiss EM10 CA transmission electron microscope.

SBEM analysis

Dataset k0725, a $50 \times 210 \times 260 \mu\text{m}$ block of fixed mouse retina imaged with voxel size $13.2 \times 13.2 \times 26 \text{ nm}$ (Ding et al., 2016) was analyzed. Manual skeletonization and annotation were performed using Knossos [<http://www.knossostool.org/>; (Helmstaedter et al., 2011)]. Tracing began at RB terminals, which were easily identified based on their size and position within the inner plexiform layer (IPL) (Mehta et al., 2014; Pallotto et al., 2015). From RB dyad synapses, AIs were traced, and then, from sites of synaptic input, ACs were traced. All skeletons and annotations were checked by two expert observers. Voxel coordinates were tilt-corrected and normalized to the positions of the ON and OFF SACs [per (Helmstaedter et al., 2011) identified in (Ding et al., 2016)]. Connectivity analysis was performed using custom-written Python scripts. Skeletons were visualized in Paraview (www.paraview.org).

Electrophysiology

All animal procedures were approved by the Institutional Animal Care and Use Committees at Yale University or the University of Maryland. Experiments used offspring of nNOS-CreER and Ai32 mice. In nNOS-CreER mice (B6; 129S-Nos1^{tm1.1(cre/ERT2)/Zjh}/J; Jackson Laboratory #014541, RRID:IMSR_JAX:014541), expression of Cre recombinase is driven by endogenous *Nos1* regulatory elements (Taniguchi et al., 2011), and Cre expression was induced by tamoxifen (2 mg delivered on two consecutive days) administered by either IP injection or gavage at P31 (SD = 5.6 days), and at least 2 weeks before the experiment. Ai32 mice (B6;129S-Gt(ROSA)26Sor^{tm32(CAG-COP4*H134R/EYFP)Hze}/J; Jackson Laboratory #024109, RRID:IMSR_JAX:024109) express a Cre-dependent channelrhodopsin-2 (ChR2)/enhanced yellow fluorescent protein (eYFP) fusion protein (Madisen et al., 2012). Ai14 mice (B6;129S6-Gt(ROSA)26Sor^{tm14(CAG-tdTomato)Hze}/J; Jackson Laboratory #007908), used for some experiments with DTA virus, express a Cre-dependent tdTomato protein (Madisen et al., 2010). Mice studied were heterozygous for the Cre allele and either the Ai32 or the Ai14 reporter allele.

A mouse aged between ~2 and 4 months was dark adapted for 1 hr, and following death, the eye was enucleated and prepared for recording in Ames medium (Sigma) under infrared light using night-vision goggles connected to a dissection microscope (Park et al., 2015). In the recording chamber, the retina was perfused (~4–6 ml/min) with warmed (31–34°C), carbogenated (95% O₂-5% CO₂) Ames' medium (light response and optogenetic experiments in whole-mount retina). The retina was imaged using a custom-built two-photon fluorescence microscope controlled with ScanImage software (RRID:SCR_014307; Borghuis et al., 2013; Borghuis et al., 2011; Pologruto et al., 2004). Fluorescent cells were targeted for whole-cell patch clamp recording with a Coherent Ultra II laser tuned to 910 nm (Park et al., 2015). For optogenetic experiments in retinal slices, dissection was performed in normal room light, and the retina was maintained in artificial CSF as described previously (Jarsky et al., 2010).

Electrophysiological measurements were made by whole-cell recordings with patch pipettes (tip resistance 4–11 MΩ). Membrane current or potential was amplified, digitized at 10–20 kHz, and stored (MultiClamp 700B amplifier; ITC-18 or Digidata 1440A A-D board) using either pClamp 10.0 (Molecular Devices) or IGOR Pro software (Wavemetrics). For light-evoked responses and optogenetic experiments in whole-mount retina, pipettes contained (in mM): 120 Cs-methanesulfonate, 5 TEA-Cl, 10 HEPES, 10 BAPTA, 3 NaCl, 2 QX-314-Cl, 4 ATP-Mg, 0.4 GTP-Na₂, and 10 phosphocreatine-Tris₂ (pH 7.3, 280 mOsm). For optogenetic experiments in retinal slices, pipettes contained (in mM): 90 Cs-methanesulfonate, 20 TEA-Cl, 1 4-AP, 10 HEPES, 1 BAPTA, 4 ATP-Mg, 0.4 GTP-Na₂, and 8 phosphocreatine-Tris₂.

Either Lucifer Yellow (0.05–0.1%) or red fluorophores (sulfarhodamine, 10 μM or Alexa 568, 60 μM) were added to the pipette solution for visualizing the cell. All drugs used for electrophysiology experiments were purchased from Tocris Biosciences, Alomone Laboratories or Sigma-Aldrich. Excitatory and inhibitory currents were recorded at holding potentials near the estimated reversal for either Cl⁻ (E_{Cl} , -67 mV) or cations (E_{cation} , +5 mV), after correcting for the liquid junction potential (-9 mV). Series resistance (~10–80 MΩ) was compensated by up to 50%. Following the recording, an image of the filled cell was acquired using 2PLSM.

Light stimuli were presented using a modified video projector [peak output, 397 nm; full-width-at-half-maximum, 20 nm (Borghuis et al., 2014; Borghuis et al., 2013) focused onto the retina through the microscope condenser. Stimuli were presented within a 4 × 3 mm area on the retina. Stimuli included contrast-reversing spots of variable diameter to measure spatial tuning (Zhang et al., 2012). For some experiments, stimuli were presented with 1 Hz temporal square-wave modulations (100% Michelson contrast) relative to a background of mean luminance that evoked ~10⁴ photoisomerizations (R*) cone⁻¹ s⁻¹ (Borghuis et al., 2014). In other experiments, stimuli were spots of dim light (4–40 R* rod⁻¹ s⁻¹) of varying diameter presented on a dark background. We did not attempt to use dimmer stimuli owing to concerns about maintaining the retina in a completely dark-adapted state over the duration of the experiment: for example targeting All ACs for recording in the whole-mount retina required exposure to infrared light sufficient to stimulate rods, albeit weakly, over a prolonged period (>10 min) and therefore precluded complete dark adaptation of the retina.

Optogenetics

ChR2-mediated responses were recorded in the presence of drugs to block conventional photoreceptor-mediated light responses. Recordings were made in a cocktail of (in μM): L-AP4 (20); either UBP310 (50) or ACET (1-5); DNQX (50-100); and D-AP5 (50–100) (Park et al., 2015). ChR2 was activated by a high-power blue LED (λ_{peak} , 450 or 470 nm; maximum intensity of ~5 × 10¹⁷ photons s⁻¹ cm⁻²) focused through the condenser onto a square (220 μm per side) area as described previously (Park et al., 2015).

Construction and production of recombinant AAV

To generate an AAV vector backbone, we modified two plasmids procured from Addgene (#62724 and #74291). We digested plasmid #74291 with BamHI, treated with Klenow fragment, digested again with HindIII, and kept the vector backbone. The insert part of plasmid #62724 was excised by digesting with EcoRI, treated with Klenow fragment, and digested again with HindIII. The excised fragment was ligated into the vector backbone from plasmid #74291. Then, we amplified the DTA

sequence by PCR, created KpnI and NheI restriction sites at each end, and subcloned the PCR products into a newly generated AAV vector. The final construct contained DTA sequence in reverse orientation surrounded by two nested pairs of incompatible loxP sites (pAAV-CAG-FLEX-NheI-DTA-KpnI-WPRE-SV40pA). The plasmid carrying DTA was obtained from Addgene (#13440).

Virus production was based on a triple-transfection, helper-free method, and the virus was purified as described previously (Byun *et al.*, 2019; Park *et al.*, 2015), except that we used a plasmid carrying AAV2/7m8 capsid (gift from Dr. John Flannery, University of California at Berkeley). The titer of the purified AAVs was determined by quantitative PCR using primers that recognize WPRE; the concentrated titers were $>10^{13}$ viral genome particles/ml in all preparations. Viral stocks were stored at -80°C .

Histology

For immunohistochemistry, animals were perfused at age 1–12 weeks. The retinas were dissected and fixed with 4% paraformaldehyde for 1 hr at 4°C . For whole-mount staining, retinas were incubated with 6% donkey serum and 0.5% triton X-100 in PBS for 1 hr at room temperature; and then incubated with 2% donkey serum and 0.5% triton X-100 in PBS with primary antibodies for 1–4 days at 4°C , and with secondary antibodies for 1–2 hr at room temperature. For morphological analysis of recorded cells, the retina was fixed for 1 hr at room temperature and reacted as described previously (Manookin *et al.*, 2008).

Primary antibodies were used at the following concentrations: goat anti-ChAT (1:200, Millipore AB144P, RRID:AB_2079751), rabbit anti-Lucifer Yellow (1:2000, ThermoFisher Scientific A-5750, RRID:AB_2536190), rabbit anti-nNOS (1:500, ThermoFisher Scientific 61–7000, RRID:AB_2533937), guinea pig anti-nNOS (1:2000, Frontier Institute Af740, RRID:AB_2571816), rabbit anti-TH (1:1000, Millipore AB152, RRID:AB_390204), rabbit anti-human/rat CRF serum (1:40,000, code #PBL rC68; gift of Dr. Paul Sawchenko, Salk Institute), guinea pig anti-LHX9 (1:20,000, gift of Dr. Jane Dodd, Columbia University). Rabbit anti-nNOS was used in all cases of nNOS immunolabeling except for **Figure 6F and G**, in which case guinea pig anti-nNOS was used. Secondary antibodies (applied for 2 hr) were conjugated to Alexa Fluor 488, Cy3 and Cy5 (Jackson ImmunoResearch or ThermoFisher Scientific) and diluted at 1:500.

Confocal imaging

Confocal imaging was performed using Zeiss laser scanning confocal microscopes (510, 710, or 800 models). For filled cells, a whole-mount image of the dendritic tree was acquired using a 20X air objective (NA = 0.8); in some cases, multiple images were combined as a montage. A high-resolution z-stack of the ChAT bands (i.e. cholinergic starburst AC processes, labeled by the ChAT antibody) and the filled amacrine or ganglion cell was obtained to determine their relative depth in the IPL using a 40X oil objective (NA = 1.4). Analysis of nNOS, Lhx9, CRH and TH antibody labeling was performed either with the 40X oil objective or the 20X air objective. Cells were counted using ImageJ (RRID:SCR_003070).

Acknowledgements

Supported by EY017836 to JHS, EY014454 and EY029323 to JBD, EY029820 to I-JK, P30-EY026878 to Yale University, a grant from the Knights Templar Eye Foundation to SJHP and an unrestricted grant from Research to Prevent Blindness to Yale University. We thank Tim Mangel and the Laboratory for Biological Ultrastructure (Department of Biology, UMD) for assistance with transmission electron microscopy, Alexander Baden for assistance with 3D visualization, and Kacie Furcolo and Adit Sabnis for assistance with SBEM dataset skeletonization. We thank Cole Graydon for comments on the manuscript.

Additional information

Funding

Funder	Grant reference number	Author
National Eye Institute	EY017836	Joshua H Singer
National Eye Institute	EY014454	Jonathan B Demb
National Eye Institute	EY029820	In-Jung Kim
National Eye Institute	P30-EY026878	In-Jung Kim Jonathan B Demb
Research to Prevent Blindness		In-Jung Kim Jonathan B Demb
National Eye Institute	EY029323	Jonathan B Demb
Knights Templar Eye Foundation		Silvia JH Park

The funders had no role in study design, data collection and interpretation, or the decision to submit the work for publication.

Author contributions

Silvia JH Park, Conceptualization, Formal analysis, Supervision, Funding acquisition, Investigation, Writing - original draft, Project administration, Writing - review and editing; Evan E Lieberman, Jiang-Bin Ke, Formal analysis, Investigation; Nao Rho, Padideh Ghorbani, Software, Investigation; Pouyan Rahmani, Investigation; Na Young Jun, Kevin L Briggman, Resources, Software, Investigation, Methodology; Hae-Lim Lee, Resources, Supervision, Funding acquisition; In-Jung Kim, Conceptualization, Supervision, Funding acquisition, Writing - original draft, Writing - review and editing; Jonathan B Demb, Conceptualization, Resources, Supervision, Funding acquisition, Writing - original draft, Writing - review and editing; Joshua H Singer, Conceptualization, Resources, Formal analysis, Supervision, Funding acquisition, Investigation, Writing - original draft, Project administration, Writing - review and editing

Author ORCIDs

Na Young Jun  <http://orcid.org/0000-0002-8841-3947>

Kevin L Briggman  <http://orcid.org/0000-0003-2946-4661>

Jonathan B Demb  <https://orcid.org/0000-0003-2227-9041>

Joshua H Singer  <https://orcid.org/0000-0002-0561-2247>

Ethics

Animal experimentation: All animal procedures were approved by the Institutional Animal Care and Use Committees at Yale University or the University of Maryland.

Decision letter and Author response

Decision letter <https://doi.org/10.7554/eLife.56077.sa1>

Author response <https://doi.org/10.7554/eLife.56077.sa2>

Additional files

Supplementary files

- Source code 1. A compressed file containing Python scripts used to parse Knossos XML files containing skeletons and annotations: see 'tutorial.py' for descriptions.
- Source data 1. Skeletons of Alls and other ACs.

- Source data 2. Skeletons of ON CBs, NOS-1 ACs, and one ON SAC.
- Source data 3. Skeletons of ON and OFF SACs.
- Transparent reporting form

Data availability

SBEM dataset k0725 is published in Ding et al. 2016. The dataset is available in the repository at <https://webknossos.org>. The dataset also can be provided on a hard drive by arrangement with Dr. Kevin L Briggman.

The following previously published dataset was used:

Author(s)	Year	Dataset title	Dataset URL	Database and Identifier
Ding H, Smith RG, Poleg-Polsky A, Diamond JS, Briggman KL	2016	k0725	https://webknossos.org/datasets/Demo_Organization/110629_k0725/view	webKnossos, 110629_k0725

References

- Ala-Laurila P**, Greschner M, Chichilnisky EJ, Rieke F. 2011. Cone photoreceptor contributions to noise and correlations in the retinal output. *Nature Neuroscience* **14**:1309–1316. DOI: <https://doi.org/10.1038/nn.2927>, PMID: 21926983
- Ala-Laurila P**, Rieke F. 2014. Coincidence detection of single-photon responses in the inner retina at the sensitivity limit of vision. *Current Biology* **24**:2888–2898. DOI: <https://doi.org/10.1016/j.cub.2014.10.028>, PMID: 25454583
- Badea TC**, Nathans J. 2004. Quantitative analysis of neuronal morphologies in the mouse retina visualized by using a genetically directed reporter. *The Journal of Comparative Neurology* **480**:331–351. DOI: <https://doi.org/10.1002/cne.20304>, PMID: 15558785
- Balasubramanian R**, Bui A, Dong X, Gan L. 2018. Lhx9 is required for the development of retinal nitric Oxide-Synthesizing amacrine cell subtype. *Molecular Neurobiology* **55**:2922–2933. DOI: <https://doi.org/10.1007/s12035-017-0554-y>, PMID: 28456934
- Beaudoin DL**, Kupershtok M, Demb JB. 2019. Selective synaptic connections in the retinal pathway for night vision. *Journal of Comparative Neurology* **527**:117–132. DOI: <https://doi.org/10.1002/cne.24313>, PMID: 28856684
- Bloomfield SA**, Xin D. 2000. Surround inhibition of mammalian All amacrine cells is generated in the proximal retina. *The Journal of Physiology* **523 Pt 3**:771–783. DOI: <https://doi.org/10.1111/j.1469-7793.2000.t01-1-00771.x>, PMID: 10718754
- Borghuis BG**, Tian L, Xu Y, Nikonov SS, Vardi N, Zemelman BV, Looger LL. 2011. Imaging light responses of targeted neuron populations in the rodent retina. *Journal of Neuroscience* **31**:2855–2867. DOI: <https://doi.org/10.1523/JNEUROSCI.6064-10.2011>, PMID: 21414907
- Borghuis BG**, Marvin JS, Looger LL, Demb JB. 2013. Two-photon imaging of nonlinear glutamate release dynamics at bipolar cell synapses in the mouse retina. *Journal of Neuroscience* **33**:10972–10985. DOI: <https://doi.org/10.1523/JNEUROSCI.1241-13.2013>, PMID: 23825403
- Borghuis BG**, Looger LL, Tomita S, Demb JB. 2014. Kainate receptors mediate signaling in both transient and sustained OFF bipolar cell pathways in mouse retina. *Journal of Neuroscience* **34**:6128–6139. DOI: <https://doi.org/10.1523/JNEUROSCI.4941-13.2014>, PMID: 24790183
- Briggman KL**, Helmstaedter M, Denk W. 2011. Wiring specificity in the direction-selectivity circuit of the retina. *Nature* **471**:183–188. DOI: <https://doi.org/10.1038/nature09818>, PMID: 21390125
- Byun H**, Lee HL, Liu H, Forrest D, Rudenko A, Kim IJ. 2019. Ror β regulates selective axon-target innervation in the mammalian midbrain. *Development* **146**:dev171926. DOI: <https://doi.org/10.1242/dev.171926>, PMID: 31332038
- Chun MH**, Oh SJ, Kim IB, Kim KY. 1999. Light and electron microscopical analysis of nitric oxide synthase-like immunoreactive neurons in the rat retina. *Visual Neuroscience* **16**:379–389. DOI: <https://doi.org/10.1017/S0952523899162175>, PMID: 10367971
- Cohen E**, Sterling P. 1990. Demonstration of cell types among cone bipolar neurons of cat retina. *Philosophical Transactions of the Royal Society of London. Series B, Biological Sciences* **330**:305–321. DOI: <https://doi.org/10.1098/rstb.1990.0201>, PMID: 1982357
- Contini M**, Raviola E. 2003. GABAergic synapses made by a retinal dopaminergic neuron. *PNAS* **100**:1358–1363. DOI: <https://doi.org/10.1073/pnas.0337681100>, PMID: 12547914
- Demb JB**, Singer JH. 2012. Intrinsic properties and functional circuitry of the All amacrine cell. *Visual Neuroscience* **29**:51–60. DOI: <https://doi.org/10.1017/S0952523811000368>, PMID: 22310372

- Demb JB**, Singer JH. 2015. Functional circuitry of the retina. *Annual Review of Vision Science* **1**:263–289. DOI: <https://doi.org/10.1146/annurev-vision-082114-035334>, PMID: 28532365
- Denk W**, Horstmann H. 2004. Serial block-face scanning electron microscopy to reconstruct three-dimensional tissue nanostructure. *PLoS Biology* **2**:e329. DOI: <https://doi.org/10.1371/journal.pbio.0020329>, PMID: 15514700
- Ding H**, Smith RG, Polog-Polsky A, Diamond JS, Briggman KL. 2016. Species-specific wiring for direction selectivity in the mammalian retina. *Nature* **535**:105–110. DOI: <https://doi.org/10.1038/nature18609>, PMID: 27350241
- Dumitrescu ON**, Pucci FG, Wong KY, Berson DM. 2009. Ectopic retinal ON bipolar cell synapses in the OFF inner plexiform layer: contacts with dopaminergic amacrine cells and melanopsin ganglion cells. *The Journal of Comparative Neurology* **517**:226–244. DOI: <https://doi.org/10.1002/cne.22158>, PMID: 19731338
- Dunn FA**, Doan T, Sampath AP, Rieke F. 2006. Controlling the gain of rod-mediated signals in the mammalian retina. *Journal of Neuroscience* **26**:3959–3970. DOI: <https://doi.org/10.1523/JNEUROSCI.5148-05.2006>, PMID: 16611812
- Dunn FA**, Rieke F. 2008. Single-photon absorptions evoke synaptic depression in the retina to extend the operational range of rod vision. *Neuron* **57**:894–904. DOI: <https://doi.org/10.1016/j.neuron.2008.01.031>, PMID: 18367090
- Famiglietti EV**, Kolb H. 1975. A bistratified amacrine cell and synaptic circuitry in the inner plexiform layer of the retina. *Brain Research* **84**:293–300. DOI: [https://doi.org/10.1016/0006-8993\(75\)90983-X](https://doi.org/10.1016/0006-8993(75)90983-X), PMID: 1111833
- Field GD**, Sampath AP, Rieke F. 2005. Retinal processing near absolute threshold: from behavior to mechanism. *Annual Review of Physiology* **67**:491–514. DOI: <https://doi.org/10.1146/annurev.physiol.67.031103.151256>, PMID: 15709967
- Graydon CW**, Lieberman EE, Rho N, Briggman KL, Singer JH, Diamond JS. 2018. Synaptic transfer between rod and cone pathways mediated by All amacrine cells in the mouse retina. *Current Biology* **28**:2739–2751. DOI: <https://doi.org/10.1016/j.cub.2018.06.063>, PMID: 30122532
- Grimes WN**, Hoon M, Briggman KL, Wong RO, Rieke F. 2014a. Cross-synaptic synchrony and transmission of signal and noise across the mouse retina. *eLife* **3**:e03892. DOI: <https://doi.org/10.7554/eLife.03892>, PMID: 25180102
- Grimes WN**, Schwartz GW, Rieke F. 2014b. The synaptic and circuit mechanisms underlying a change in spatial encoding in the retina. *Neuron* **82**:460–473. DOI: <https://doi.org/10.1016/j.neuron.2014.02.037>, PMID: 24742466
- Grimes WN**, Graves LR, Summers MT, Rieke F. 2015. A simple retinal mechanism contributes to perceptual interactions between rod- and cone-mediated responses in primates. *eLife* **4**:e08033. DOI: <https://doi.org/10.7554/eLife.08033>, PMID: 26098124
- Grimes WN**, Baudin J, Azevedo AW, Rieke F. 2018a. Range, routing and kinetics of rod signaling in primate retina. *eLife* **7**:e38281. DOI: <https://doi.org/10.7554/eLife.38281>, PMID: 30299254
- Grimes WN**, Songco-Aguas A, Rieke F. 2018b. Parallel processing of rod and cone signals: retinal function and human perception. *Annual Review of Vision Science* **4**:123–141. DOI: <https://doi.org/10.1146/annurev-vision-091517-034055>, PMID: 29883274
- Gustincich S**, Feigenspan A, Wu DK, Koopman LJ, Raviola E. 1997. Control of dopamine release in the retina: a transgenic approach to neural networks. *Neuron* **18**:723–736. DOI: [https://doi.org/10.1016/S0896-6273\(00\)80313-X](https://doi.org/10.1016/S0896-6273(00)80313-X), PMID: 9182798
- Hartveit E**, Veruki ML. 2012. Electrical synapses between All amacrine cells in the retina: function and modulation. *Brain Research* **1487**:160–172. DOI: <https://doi.org/10.1016/j.brainres.2012.05.060>, PMID: 22776293
- Helmstaedter M**, Briggman KL, Denk W. 2011. High-accuracy neurite reconstruction for high-throughput neuroanatomy. *Nature Neuroscience* **14**:1081–1088. DOI: <https://doi.org/10.1038/nn.2868>, PMID: 21743472
- Helmstaedter M**, Briggman KL, Turaga SC, Jain V, Seung HS, Denk W. 2013. Connectomic reconstruction of the inner plexiform layer in the mouse retina. *Nature* **500**:168–174. DOI: <https://doi.org/10.1038/nature12346>, PMID: 23925239
- Hoggarth A**, McLaughlin AJ, Ronellenfitch K, Trenholm S, Vasandani R, Sethuramanujam S, Schwab D, Briggman KL, Awatramani GB. 2015. Specific wiring of distinct amacrine cells in the directionally selective retinal circuit permits independent coding of direction and size. *Neuron* **86**:276–291. DOI: <https://doi.org/10.1016/j.neuron.2015.02.035>, PMID: 25801705
- Hoshi H**, Liu WL, Massey SC, Mills SL. 2009. ON inputs to the OFF layer: bipolar cells that break the stratification rules of the retina. *Journal of Neuroscience* **29**:8875–8883. DOI: <https://doi.org/10.1523/JNEUROSCI.0912-09.2009>, PMID: 19605625
- Hsiang JC**, Johnson KP, Madisen L, Zeng H, Kerschensteiner D. 2017. Local processing in neurites of VGluT3-expressing amacrine cells differentially organizes visual information. *eLife* **6**:e31307. DOI: <https://doi.org/10.7554/eLife.31307>, PMID: 29022876
- Ingram NT**, Sampath AP, Fain GL. 2016. Why are rods more sensitive than cones? *The Journal of Physiology* **594**:5415–5426. DOI: <https://doi.org/10.1113/JP272556>, PMID: 27218707
- Jacoby J**, Zhu Y, DeVries SH, Schwartz GW. 2015. An amacrine cell circuit for signaling steady illumination in the retina. *Cell Reports* **13**:2663–2670. DOI: <https://doi.org/10.1016/j.celrep.2015.11.062>, PMID: 26711334
- Jacoby J**, Nath A, Jessen ZF, Schwartz GW. 2018. A Self-Regulating gap junction network of amacrine cells controls nitric oxide release in the retina. *Neuron* **100**:1149–1162. DOI: <https://doi.org/10.1016/j.neuron.2018.09.047>, PMID: 30482690

- Jarsky T**, Tian M, Singer JH. 2010. Nanodomain control of exocytosis is responsible for the signaling capability of a retinal ribbon synapse. *Journal of Neuroscience* **30**:11885–11895. DOI: <https://doi.org/10.1523/JNEUROSCI.1415-10.2010>, PMID: 20826653
- Johnson J**, Sherry DM, Liu X, Fremereau RT, Seal RP, Edwards RH, Copenhagen DR. 2004. Vesicular glutamate transporter 3 expression identifies glutamatergic amacrine cells in the rodent retina. *The Journal of Comparative Neurology* **477**:386–398. DOI: <https://doi.org/10.1002/cne.20250>, PMID: 15329888
- Ke J-B**, Wang YV, Borghuis BG, Cembrowski MS, Riecke H, Kath WL, Demb JB, Singer JH. 2014. Adaptation to background light enables contrast coding at rod bipolar cell synapses. *Neuron* **81**:13–401. DOI: <https://doi.org/10.1016/j.neuron.2013.10.054>
- Kim IB**, Lee EJ, Kim KY, Ju WK, Oh SJ, Joo CK, Chun MH. 1999. Immunocytochemical localization of nitric oxide synthase in the mammalian retina. *Neuroscience Letters* **267**:193–196. DOI: [https://doi.org/10.1016/S0304-3940\(99\)00363-8](https://doi.org/10.1016/S0304-3940(99)00363-8), PMID: 10381009
- Kim HL**, Jeon JH, Koo TH, Lee UY, Jeong E, Chun MH, Moon JI, Massey SC, Kim IB. 2012. Axonal synapses utilize multiple synaptic ribbons in the mammalian retina. *PLOS ONE* **7**:e52295. DOI: <https://doi.org/10.1371/journal.pone.0052295>, PMID: 23284975
- Kim T**, Soto F, Kerschensteiner D. 2015. An excitatory amacrine cell detects object motion and provides feature-selective input to ganglion cells in the mouse retina. *eLife* **4** e08025. DOI: <https://doi.org/10.7554/eLife.08025>
- Kuo SP**, Schwartz GW, Rieke F. 2016. Nonlinear spatiotemporal integration by electrical and chemical synapses in the retina. *Neuron* **90**:320–332. DOI: <https://doi.org/10.1016/j.neuron.2016.03.012>
- Lauritzen JS**, Anderson JR, Jones BW, Watt CB, Mohammed S, Hoang JV, Marc RE. 2013. ON cone bipolar cell axonal synapses in the OFF inner plexiform layer of the rabbit retina. *Journal of Comparative Neurology* **521**:977–1000. DOI: <https://doi.org/10.1002/cne.23244>, PMID: 23042441
- Lauritzen JS**, Sigulinsky CL, Anderson JR, Kalloniatis M, Nelson NT, Emrich DP, Rapp C, McCarthy N, Kerzner E, Meyer M, Jones BW, Marc RE. 2019. Rod-cone crossover connectome of mammalian bipolar cells. *Journal of Comparative Neurology* **527**:87–116. DOI: <https://doi.org/10.1002/cne.24084>, PMID: 27447117
- Lee S**, Zhang Y, Chen M, Zhou ZJ. 2016. Segregated Glycine-Glutamate Co-transmission from vGluT3 amacrine cells to Contrast-Suppressed and Contrast-Enhanced retinal circuits. *Neuron* **90**:27–34. DOI: <https://doi.org/10.1016/j.neuron.2016.02.023>, PMID: 26996083
- Lin B**, Masland RH. 2006. Populations of wide-field amacrine cells in the mouse retina. *The Journal of Comparative Neurology* **499**:797–809. DOI: <https://doi.org/10.1002/cne.21126>, PMID: 17048228
- Madisen L**, Zwingman TA, Sunkin SM, Oh SW, Zariwala HA, Gu H, Ng LL, Palmiter RD, Hawrylycz MJ, Jones AR, Lein ES, Zeng H. 2010. A robust and high-throughput cre reporting and characterization system for the whole mouse brain. *Nature Neuroscience* **13**:133–140. DOI: <https://doi.org/10.1038/nn.2467>, PMID: 20023653
- Madisen L**, Mao T, Koch H, Zhuo JM, Berenyi A, Fujisawa S, Hsu YW, Garcia AJ, Gu X, Zanella S, Kidney J, Gu H, Mao Y, Hooks BM, Boyden ES, Buzsáki G, Ramirez JM, Jones AR, Svoboda K, Han X, et al. 2012. A toolbox of Cre-dependent optogenetic transgenic mice for light-induced activation and silencing. *Nature Neuroscience* **15**:793–802. DOI: <https://doi.org/10.1038/nn.3078>, PMID: 22446880
- Manookin MB**, Beaudoin DL, Ernst ZR, Flagel LJ, Demb JB. 2008. Disinhibition combines with excitation to extend the operating range of the OFF visual pathway in daylight. *Journal of Neuroscience* **28**:4136–4150. DOI: <https://doi.org/10.1523/JNEUROSCI.4274-07.2008>, PMID: 18417693
- Mehta B**, Ke JB, Zhang L, Baden AD, Markowitz AL, Nayak S, Briggman KL, Zenisek D, Singer JH. 2014. Global Ca²⁺ signaling drives ribbon-independent synaptic transmission at rod bipolar cell synapses. *Journal of Neuroscience* **34**:6233–6244. DOI: <https://doi.org/10.1523/JNEUROSCI.5324-13.2014>, PMID: 24790194
- Mills SL**, Massey SC. 1995. Differential properties of two gap junctional pathways made by All amacrine cells. *Nature* **377**:734–737. DOI: <https://doi.org/10.1038/377734a0>
- Mortensen LS**, Park SJH, Ke JB, Cooper BH, Zhang L, Imig C, Löwel S, Reim K, Brose N, Demb JB, Rhee JS, Singer JH. 2016. Complexin 3 increases the fidelity of signaling in a retinal circuit by regulating exocytosis at ribbon synapses. *Cell Reports* **15**:2239–2250. DOI: <https://doi.org/10.1016/j.celrep.2016.05.012>, PMID: 27239031
- Murphy GJ**, Rieke F. 2006. Network variability limits stimulus-evoked spike timing precision in retinal ganglion cells. *Neuron* **52**:511–524. DOI: <https://doi.org/10.1016/j.neuron.2006.09.014>, PMID: 17088216
- Murphy GJ**, Rieke F. 2008. Signals and noise in an inhibitory interneuron diverge to control activity in nearby retinal ganglion cells. *Nature Neuroscience* **11**:318–326. DOI: <https://doi.org/10.1038/nn2045>, PMID: 18223648
- Nelson R**. 1982. All amacrine cells quicken time course of rod signals in the cat retina. *Journal of Neurophysiology* **47**:928–947. DOI: <https://doi.org/10.1152/jn.1982.47.5.928>, PMID: 6177841
- Palotto M**, Watkins PV, Fubara B, Singer JH, Briggman KL. 2015. Extracellular space preservation aids the connectomic analysis of neural circuits. *eLife* **4** e08206. DOI: <https://doi.org/10.7554/eLife.08206>, PMID: 26650352
- Park SJ**, Borghuis BG, Rahmani P, Zeng Q, Kim IJ, Demb JB. 2015. Function and circuitry of VIP+ interneurons in the mouse retina. *Journal of Neuroscience* **35**:10685–10700. DOI: <https://doi.org/10.1523/JNEUROSCI.0222-15.2015>, PMID: 26224854
- Park SJH**, Pottackal J, Ke JB, Jun NY, Rahmani P, Kim IJ, Singer JH, Demb JB. 2018. Convergence and divergence of CRH amacrine cells in mouse retinal circuitry. *The Journal of Neuroscience* **38**:3753–3766. DOI: <https://doi.org/10.1523/JNEUROSCI.2518-17.2018>, PMID: 29572434
- Pérez De Sevilla Müller L**, Shelley J, Weiler R. 2007. Displaced amacrine cells of the mouse retina. *The Journal of Comparative Neurology* **505**:177–189. DOI: <https://doi.org/10.1002/cne.21487>, PMID: 17853452

- Pologruto TA**, Yasuda R, Svoboda K. 2004. Monitoring neural activity and [Ca²⁺] with genetically encoded Ca²⁺ indicators. *Journal of Neuroscience* **24**:9572–9579. DOI: <https://doi.org/10.1523/JNEUROSCI.2854-04.2004>, PMID: 15509744
- Pugh EN**. 2018. The discovery of the ability of rod photoreceptors to signal single photons. *Journal of General Physiology* **150**:383–388. DOI: <https://doi.org/10.1085/jgp.201711970>, PMID: 29467164
- Sabbah S**, Berg D, Papendorp C, Briggman KL, Berson DM. 2017. A cre mouse line for probing irradiance- and Direction-Encoding retinal networks. *Eneuro* **4**:ENEURO.0065-17.2017. DOI: <https://doi.org/10.1523/ENEURO.0065-17.2017>, PMID: 28466070
- Schwartz GW**, Okawa H, Dunn FA, Morgan JL, Kerschensteiner D, Wong RO, Rieke F. 2012. The spatial structure of a nonlinear receptive field. *Nature Neuroscience* **15**:1572–1580. DOI: <https://doi.org/10.1038/nn.3225>, PMID: 23001060
- Slaughter MM**, Miller RF. 1981. 2-amino-4-phosphonobutyric acid: a new pharmacological tool for retina research. *Science* **211**:182–185. DOI: <https://doi.org/10.1126/science.6255566>, PMID: 6255566
- Smeds L**, Takeshita D, Turunen T, Tiihonen J, Westö J, Martyniuk N, Seppänen A, Ala-Laurila P. 2019. Paradoxical rules of spike train decoding revealed at the sensitivity limit of vision. *Neuron* **104**:576–587. DOI: <https://doi.org/10.1016/j.neuron.2019.08.005>
- Stabio ME**, Sabbah S, Quattrochi LE, Ilardi MC, Fogerson PM, Leyrer ML, Kim MT, Kim I, Schiel M, Renna JM, Briggman KL, Berson DM. 2018. The M5 cell: a Color-Opponent intrinsically photosensitive retinal ganglion cell. *Neuron* **97**:251. DOI: <https://doi.org/10.1016/j.neuron.2017.12.030>, PMID: 29301102
- Strettoi E**, Dacheux RF, Raviola E. 1990. Synaptic connections of rod bipolar cells in the inner plexiform layer of the rabbit retina. *The Journal of Comparative Neurology* **295**:449–466. DOI: <https://doi.org/10.1002/cne.902950309>, PMID: 2351763
- Strettoi E**, Raviola E, Dacheux RF. 1992. Synaptic connections of the narrow-field, bistratified rod amacrine cell (All) in the rabbit retina. *The Journal of Comparative Neurology* **325**:152–168. DOI: <https://doi.org/10.1002/cne.903250203>, PMID: 1460111
- Strettoi E**, Dacheux RF, Raviola E. 1994. Cone bipolar cells as interneurons in the rod pathway of the rabbit retina. *The Journal of Comparative Neurology* **347**:139–149. DOI: <https://doi.org/10.1002/cne.903470111>, PMID: 7798378
- Taniguchi H**, He M, Wu P, Kim S, Paik R, Sugino K, Kvitsani D, Kvitsani D, Fu Y, Lu J, Lin Y, Miyoshi G, Shima Y, Fishell G, Nelson SB, Huang ZJ. 2011. A resource of cre driver lines for genetic targeting of GABAergic neurons in cerebral cortex. *Neuron* **71**:995–1013. DOI: <https://doi.org/10.1016/j.neuron.2011.07.026>, PMID: 21943598
- Tien N-W**, Soto F, Kerschensteiner D. 2017. Homeostatic plasticity shapes Cell-Type-Specific wiring in the retina. *Neuron* **94**:656–665. DOI: <https://doi.org/10.1016/j.neuron.2017.04.016>
- Tsakamoto Y**, Omi N. 2013. Functional allocation of synaptic contacts in microcircuits from rods via rod bipolar to All amacrine cells in the mouse retina. *Journal of Comparative Neurology* **521**:3541–3555. DOI: <https://doi.org/10.1002/cne.23370>, PMID: 23749582
- Voigt T**, Wässle H. 1987. Dopaminergic innervation of A II amacrine cells in mammalian retina. *The Journal of Neuroscience* **7**:4115–4128. DOI: <https://doi.org/10.1523/JNEUROSCI.07-12-04115.1987>, PMID: 2891802
- Xin D**, Bloomfield SA. 1999. Comparison of the responses of All amacrine cells in the dark- and light-adapted rabbit retina. *Visual Neuroscience* **16**:653–665. DOI: <https://doi.org/10.1017/S0952523899164058>, PMID: 10431914
- Yan W**, Laboulaye MA, Tran NM, Whitney IE, Benhar I, Sanes JR. 2020. Molecular identification of sixty-three amacrine cell types completes a mouse retinal cell atlas. *bioRxiv*. DOI: <https://doi.org/10.1101/2020.03.10.985770>
- Zhang Y**, Kim IJ, Sanes JR, Meister M. 2012. The most numerous ganglion cell type of the mouse retina is a selective feature detector. *PNAS* **109**:E2391–E2398. DOI: <https://doi.org/10.1073/pnas.1211547109>, PMID: 22891316
- Zhu Y**, Xu J, Hauswirth WW, DeVries SH. 2014. Genetically targeted binary labeling of retinal neurons. *Journal of Neuroscience* **34**:7845–7861. DOI: <https://doi.org/10.1523/JNEUROSCI.2960-13.2014>, PMID: 24899708